Electrocatalytic Ammonia Oxidation with a Tailored Molecular Catalyst Heterogenized via Surface Host-Guest Complexation

Helena Roithmeyer[a], Laurent Sévery[a,b], Thomas Moehl[a], Bernhard Spingler[a], Olivier Blacque[a], Thomas Fox[a], Marcella Iannuzzi[a] and S. David Tilley[a]*

[a]Department of Chemistry, University of Zurich, Winterthurerstrasse 190, 8057, Zurich, Switzerland

ABSTRACT: Macrocyclic host molecules bound to electrode surfaces enable the complexation of catalytically active guests for molecular heterogeneous catalysis. We present a surface-anchored host-guest complex with the ability to electrochemically oxidize ammonia in both organic and aqueous solutions. With an adamantyl motif as the binding group on the backbone of the molecular catalyst [Ru(bpy-NMe_2)(tpada)(Cl)](PF_6) (**1**) (where bpy-NMe_2 is 4,4'-bis(dimethylamino)-2,2'-bipyridyl, tpada is 4'-(adamantan-1-yl)-2,2':6',2"-terpyridine), high binding constants with β-cyclodextrin were observed in solution (in dmso-d_6: D_2O (7:3), K_{11} = 1581 ± 95 M^{-1}). The strong binding affinities also transferred to a mesoporous ITO (mITO) surface functionalized with a phosphonated derivative of β-cyclodextrin. The newly designed catalyst (**1**) was compared to the previously reported naphthyl-substituted catalyst [Ru(bpy-NMe_2)(tpnp)(Cl)](PF_6) (**2**) (where tpnp is 4'-(naphthalene-2-yl)-2,2':6',2"-terpyridine) for its stability during catalysis. Despite the insulating nature of the adamantyl substituent serving as the binding group, the stronger binding of this unit to the host functionalized electrode and the resulting shorter distance between the catalytic active center and the surface led to better performance and higher stability. Both guests are able to oxidize ammonia in both organic and aqueous solutions and the host-anchored electrode can be refunctionalized multiple times (>3) following loss of the catalytic activity, without a reduction in performance. Guest **1** exhibits significantly higher stability in comparison to guest **2** towards basic conditions, which often constitutes a challenge for anchored molecular systems. Ammonia oxidation in water led to the selective formation of NO_3^- with faradaic efficiencies of up to 98%.

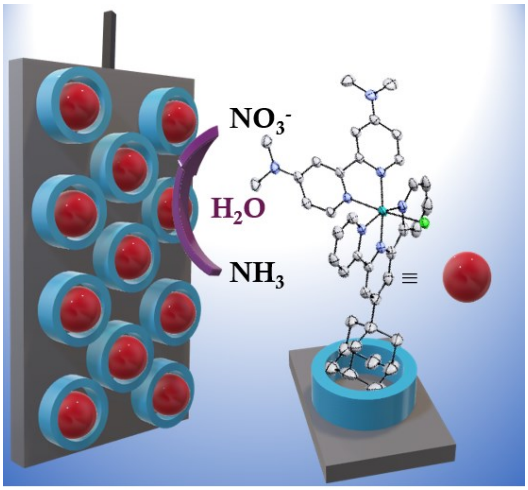

Figure TOC: Ammonia oxidation with a surface-bound host-guest system, yielding NO_3^- in aqueous solution.

INTRODUCTION

The increasing demand for energy carriers from sustainable sources drives the search for fossil fuel-free alternatives. Ammonia is a carbon-free energy carrier for molecular hydrogen and has significant practical benefits such as liquefaction under mild conditions and high volumetric energy density.[1] NH_3 has also been proposed as a medium for energy storage to directly power fuel cells.[2,3]

Realizing NH_3 as a carbon-free alternative fuel requires the development of efficient catalytic conversion strategies between ammonia and molecular hydrogen in both directions. With a potential of +0.092 V (vs. NHE, pH=0) for ammonia oxidation (AO) in water, it is relatively mild in comparison to water oxidation.

One of the main challenges is the optimization of the selectivity and reduction of the required overpotential. While the reduction of N_2 to NH_3 has been studied extensively, the development of molecular ammonia oxidation catalysts has only recently started gaining attention.[4,5] Several molecular electrocatalysts have been developed to convert ammonia to dinitrogen and hydrogen, the reverse of the Haber-Bosch process. In particular, ruthenium-based molecular catalysts were investigated by several groups, including the ones of Llobet and Bullock.[6–8] Very recently, the application of non-noble metal-based catalysts, such as iron, nickel and copper, has been explored, opening the possibilities for catalysis with more sustainable systems.[9–15] Along with the discovery of non-noble metal based catalysts for AO, the replacement of organic solvents with water was investigated. In 2022, the group of Brudvig demonstrated the electrocatalytic transformation of NH_3 to NO_2^- and NO_3^- in a homogeneous electro-catalytic approach with a Cu-complex, with high faradaic efficiencies.[16]

Ammonia oxidation in water is not only environmentally friendlier but also offers the opportunity to release 4 equivalents of H_2 per ammonia molecule while forming a value-added product (NO_3^-), which is used in fertilizers. Fertilizer production dominates the industrial use of nitric acid with almost 81%, however, its synthesis via the Ostwald process is highly energy demanding.[17,18]

Molecular electrocatalysts show high activity in comparison to heterogeneous catalysts but suffer from reduced stability. The high pH of aqueous ammonia solutions presents an additional challenge for the stability of these catalysts. While thus far, the reported homogeneous catalysts exhibit large overpotentials, tuning of the metal ion and ligand sphere provides a powerful method for improving the performance. Heterogenization by immobilization of a molecular catalyst onto an electrode via a host-guest (HG) complex can be beneficial as this combines the high activity of molecular catalysts with the high stability of heterogeneous catalysts. Moreover, diffusion limitations of homogeneous catalysts in electrolytic systems may be overcome since all catalyst molecules are bound to the electrode surface, dramatically reducing the amount of catalyst present in the system compared to homogeneous systems. Beiler et al. recently reported a heterogenized approach anchoring a Ru-bda oligomer as the catalyst to the electrode via π-interactions, which showed high turnover numbers and faradaic efficiencies.[19] A clear benefit of the anchored catalyst is that electrocatalysis can be conducted in an aqueous medium. However, the system displayed

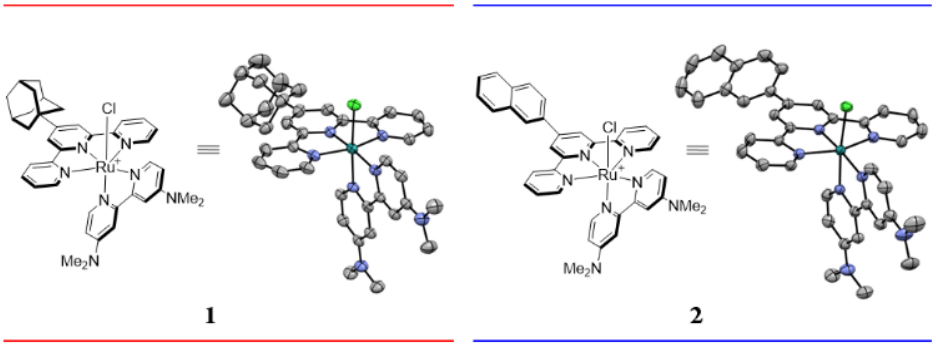

Figure 1: ORTEP structures of the guest molecules **1** and **2**. Ellipsoids are drawn at 50% probability. Solvent molecules, hydrogens and anionic species (PF_6^-) are omitted for clarity.

limited stability at higher pH (>10). Increasing the stability of the system while maintaining high efficiency could be achieved by employing a supramolecular HG assembly bound to the electrode surface. The HG complex enables the flow of charge between the surface and the catalytically active metal center. As reported previously,[20] the HG electrochemical approach benefits from a non-direct bond from the surface to the catalysts, which allows for electrode recyclability and the independent improvement of the host anchoring unit, the guest binding group, and its desired active metal center. Tailoring the HG systems can lead to increased stability of molecular catalysts. In our previous work, we modified the backbone of the known $[Ru(tpy)(bpy\text{-}NMe_2)]^{2+}$ (where bpy-NMe_2 is 4,4'-bis(dimethylamino)-2,2'-bipyridyl and tpy is terpyridine) catalyst with an aromatic unit (naphthyl) to enable the flow of electrons between the catalytic active species and the electrode surface (guest **2**).[20] In the present study, we show that the catalyst backbone (guest **1**) does not necessarily need to exhibit electron-transporting functionalities as long as the distance from the active site of the catalyst to the surface is sufficiently short to enable electron transfer via tunneling. We sought to improve our catalytic system by introducing a binding group to the guest molecules that typically exhibit stronger HG complex formation with beta-cyclodextrins (β-CD). Adamantane derivatives were reported to be among the strongest guests to bind to β-CD in (aqueous) solution,[21–23] which motivated the incorporation of an adamantyl-substituent on the terpyridine backbone of the guest (**Figure 1)**. With this, we aimed to transfer the excellent binding properties from the solution to the surface-bound host molecule to achieve strong yet reversible binding of the catalyst guests on an electrode for efficient ammonia oxidation.

RESULTS AND DISCUSSION

Herein, we present the synthesis of a new ammonia oxidation catalyst $[Ru(bpy\text{-}NMe_2)(tpada)(Cl)](PF_6)$ (**1**), with an adamantane binding group that can form a catalytically active HG complex on an electrode surface. Guest **1** was synthesized in a two-step reaction with the newly designed terpyridine-adamantyl (tpada) ligand (**Schemes S1-2, Figures S1-2**), $RuCl_3$ and 4,4'-bis(dimethylamino)-2,2'-bipyridine (bpy-NMe_2) (**Scheme S3, Figures S3-7).** The related adamantane-containing complex $[Ru(bpy)(tpada)\text{-}(Cl)](PF_6)$ (**3**) (**Scheme S4, Figures S8-13)** with unsubstituted bpy instead of bpy-NMe_2 exhibited a later onset potential for ammonia oxidation and was therefore not investigated further.

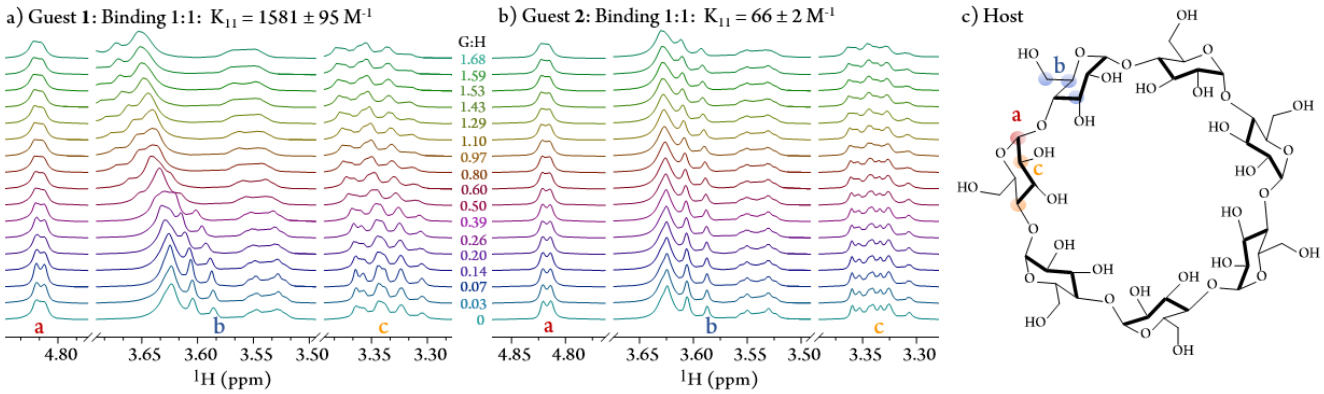

Figure 2: ^{1}H NMR titration of guests **1** (a) and guest **2** (b) with β-CD (c) as the host in dmso-d_6: D_2O (7:3) at 298 K with a constant host concentration of 0.001 M. The proton assignment of the host was done according to literature.[24] The hydroxy units are not visible due to the fast exchange with D_2O. The guest ratio is increased from 0 to 1.68 relative to the host concentration (from bottom to top). The binding constants were obtained using BindFit.[25,26]

With a cavity size of β-CD of 0.65 nm and a length of 0.78 nm, the smaller adamantyl guest can be bound more easily than the larger naphthyl guest.[27,28] The binding of both guests **1** and **2** to β-CD in a dmso-d_6: D_2O (7:3) solution was monitored with ^{1}H NMR spectroscopy, and titration studies (**Figure 2**) used to determine the solution-phase binding-constant. The binding behavior of both guests was compared by fitting the chemical shift change of the host protons and the H/G ratio with BindFit (**Figures S14-S16**).[26,29] A more pronounced peak shift of the cyclodextrin protons assigned to protons b **(Figure 2c)** was observed when titrating guest **1** in comparison to guest **2**, which implies a stronger interaction of the adamantane backbone with the host. We found a binding constant of K_{11}= 1581 ± 95 M^{-1} for the 1:1 inclusion complex of guest **1** with the β-CD host, which is more than 20 times higher than the one obtained for guest **2** (K_{11}= 66 ± 2 M^{-1}). These results suggest that the newly designed HG system could show higher stability during catalysis if the strong binding of the guest is transferred to the electrode surface.

To evaluate the stability of the HG complex anchored to the oxide surface, we have created atomistic models for both guests **1** and **2 (Figure 3)**.

All simulations have been performed by means of the Gaussian and plane waves method as implemented in the CP2K program package.[30] The structures, simulated by density functional theory (DFT), consist of an oxide slab of six layers of rutile TiO_2 (110) to which the bisphosphonated cyclodextrin macrocycle has been adsorbed on one side. On both sides, the free oxide surface has been covered by a ~5 Å thick film of liquid water, while the guest complex has been introduced into the empty host cavity. The whole system was first equilibrated at room temperature by ab initio molecular dynamic (AIMD) simulations for a few picoseconds. Then the structure was optimized starting from one AIMD snapshot. Energetics and electronic properties were finally evaluated at the hybrid functional level of theory (**Figure S17**). The optimization of both guests **1** and **2** showed that guest **1** binds slightly stronger to the surface-bound host (-6.97 eV vs. -6.67 eV) (**Figure 3**). Both guest molecules interact with the host, but no hybridization with the substrate orbitals is observed, in contrast to our previous report on gold.[20]

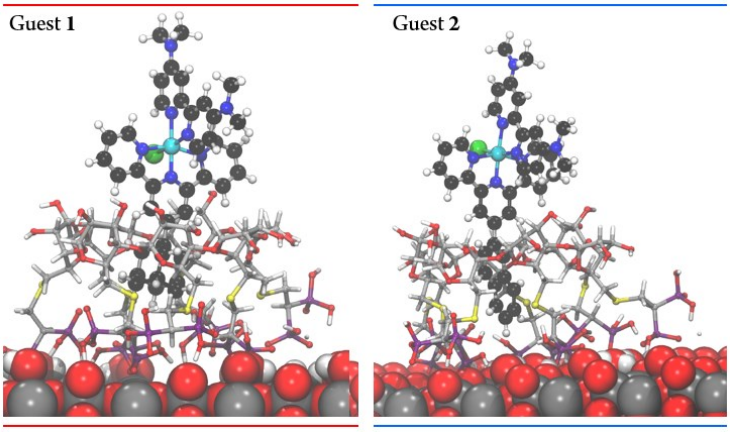

Figure 3: DFT optimized structure of the guest **1** (left) and guest **2** (right) interacting with the TiO_2 (110) surface-bound host. Most of the water molecules have been removed from the illustration for the sake of clarity, thus leaving only the ones adsorbed at the surface.

To study whether the binding group influences the catalytic performance and stability, guests **1** and **2** were compared during electrocatalysis. To this end, electrodes functionalized with the HG-bound molecular catalysts were prepared. β-CD was functionalized and bound to a mesoporous indium tin oxide (mITO) electrode surface (**Figure S18**) as reported previously.[20] The modified bisphosphonated cyclodextrin macrocycle can bind to the mITO substrate with up to 28 bonds, forming a stable surface-anchored host cavity. For electrocatalysis, the mITO electrode was modified with the host and afterwards dipped for 1 h in a solution of 0.1 mM of each of the guest complexes **1** and **2** in MeOH to form the HG complex (**Figure S19**). The functionalized electrodes were analyzed by cyclic voltammetry (CV) (**Figure S20**) in THF or aqueous solution (set up **Figure S21-22**) with and without ammonia to assess general electrochemical and catalytic properties for the oxidation of ammonia.

The formation of the HG complex could be confirmed by CV (**Figure 4a**) and UV/Vis spectroscopy (**Figure S23**) and is also visible to the naked eye in the form of electrode surface staining after HG formation. The observation of the redox peaks of the guests indicates that electron transfer between the catalysts and the electrode surface is possible. The redox couples of guest **1** are observable at around - 0.09 V vs. Fc/Fc^+ for the Ru (II/III) oxidation (**Figure 4a** red), whereas guest **2** shows its related redox peak at more positive potentials (**Figure 4a** blue), which is likely due to a ligand exchange.

In 0.5 M ammonia solution (THF) (**Figure 4b**), an onset for ammonia oxidation with both guests can be observed at around - 0.22 V vs Fc/Fc^+ in comparison to the blank without a guest (mITO + host, **Figure 4b,** black dashed line), which shows a slightly earlier onset and higher current for guest **1** (red). The difference in current is attributed to catalyst loading. Guest **1** exhibits a higher amount of immobilized catalyst (0.026 mC), which can be determined from the integration of the redox peaks (**Figure S24**) and which corresponds to a catalyst loading of 1.14 pmol cm^{-2} in comparison to guest **2,** exhibiting 0.015 mC and a surface loading of 0.66 pmol cm^{-2}. The higher surface loading of guest **1** could be due to its slightly smaller size, which enables the catalyst to better infiltrate the mesoporous structure of the electrode.

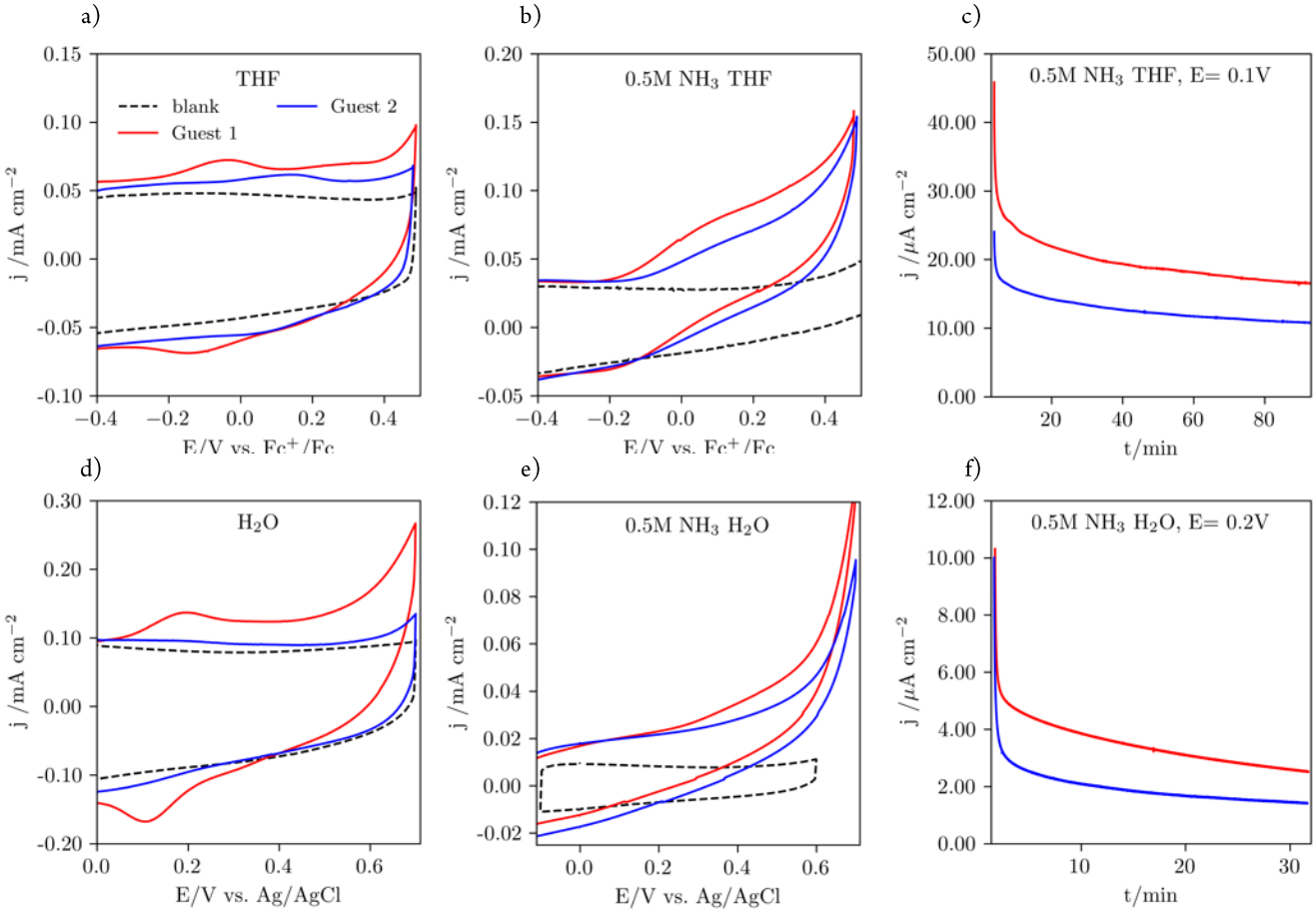

Figure 4: Electrochemistry of guest **1** (G1, red) and guest **2** (G2, blue) in THF (a-c) and water (d-e), blank (dashed black line, WE: mITO+Host). **THF:** a) CV (100 mV/s) in 0.1 M $TBAPF_6$ in THF. b) CV (20 mVs^{-1}) in 0.1 M $TBAPF_6$, 0.1 M NH_4PF_6 0.5 M NH_3 in THF and c) CA for 90 min at 0.1 V vs Fc^+/Fc. Conditions: WE: mITO+Host+Guest, CE: Pt wire, RE: AgCl wire in 0.1M $TBAPF_6$ in THF. **H_2O:** d) CV (100 mVs^{-1}) in 0.2 M $NaClO_4$ in H_2O e) CV (20 mVs^{-1}) in 0.2 M $NaClO_4$, 0.5 M NH_3 in H_2O (pH= 11.3 at 22 °C) and f) CA for 30 min in 0.2 M $NaClO_4$, 0.5 M NH_3 in H_2O, at. 0.2 V vs. Ag/AgCl. Conditions: WE: mITO+Host+Guest, CE: Pt, RE: Ag/AgCl wire in 0.2M $NaClO_4$ in H_2O. The graphs are plotted to the geometric surface area. The surface loading is calculated according to the electrochemically determined surface area (SI p. S36).

Chronoamperometry (CA) was employed to gain information on the stability of the HG-immobilized assembly during electrocatalysis. The applied potential was set to 0.1 V vs Fc/Fc^+ in THF, which is slightly more oxidative than the Ru(II)/Ru(III) oxidation peak of guest **2**. After 90 min of operation (in 0.5 M NH_3 in THF) (**Figure 4c**), the electrode functionalized with guest **1** (red) retained more current over time compared to a guest **2**-functionalized electrode (blue). This indicates a more robust connection between the adamantyl-substituted guest and the surface-bound hosts, which correlates with the stronger binding observed in solution. Additionally, higher currents were observable for guest **1**, which can be explained by the higher surface loading. When comparing CV and CA of the electrodes with physisorbed guest **1** (**Figure S25**), which lacks the host functionalization, no redox peak or catalytic activity was observed, which indirectly confirms the formation of the HG complex in the presence of a host-functionalized surface.

After extensive efforts to detect the evolved N_2 with gas chromatography (GC) we were unable to unambiguously confirm that N_2 was produced from the catalysis due to an unavoidable air leak that was large in comparison to the theoretically produced N_2, as the catalyst is in the range of picomolar per cm^2.

We then switched our focus to the more practical aqueous system. In aqueous solution (supporting electrolyte 0.2 M $NaClO_4$), guest **1** is reversibly oxidized (Ru II/III) at 0.14 V vs Ag/AgCl (**Figure 4d**). Additionally, we found that our systems are active in water, even without the addition of supporting electrolytes, in 0.5 M NH_3 solution resulting in a pH of 11.3. An onset for AO in 0.5 M NH_3 can be seen at 0 V vs Ag/AgCl (**Figure 4e**). For guest **2,** only a very weak redox peak at 0.27 V was observable, which could again be a broad overlapping peak from RuII/III and RuIII/IV. However, the onset for ammonia oxidation was noticed at a similar potential for both guests (**Figure 4e**), though similar to the experiment in organic solvent, less pronounced for guest **2**.

GCMS with labeled $^{15}NH_3$ solution (0.5 M in H_2O) did not show any conversion to $^{30}N_2$ (**Figures S27** and **S28**), which led us to the assumption that different products must be formed in water. Inspired by the work of Liu et al.[16] we tested our systems with the Griess test (**Figures S29-S34**) after electrocatalysis to determine the formation of NO_2^- and NO_3^- in water. Selective conversion of NH_3 to NO_3^- was achieved when applying 0.5 V vs Ag/AgCl for 90 min in 200 mM NH_3 in aqueous phosphate buffer (pH= 10.86) (**Figure S35**). Guest **1**, showed high stability at pH 10.86 and a FE of 96% with a TON of 1263. Guest **2**, showed varying values, with an average FE of 69% and a TON of 1130, which could be due to the high pH conditions and therefore faster desorption from the binding pocket. Thereby, the catalyst loading on the surface is limiting the charge flow and the FE. Proton decoupled ^{14}N NMR studies of the anolyte solution exhibited the presence of a single peak at 371 ppm (**Figure S36**), which can be assigned to NO_3^- in basic conditions (pH 11) as referenced by a standard KNO_3 sample.

To rationalize the better catalytic performance of guest **1** despite the insulating nature of the adamantane binding group, we performed potential step experiments from 0 V to 0.2 V (vs. open circuit) (oxidation) and from 0 to –0.2 V (vs. open circuit) (reduction) (**Figure S37**) and calculated the electron transfer rate constants for both guests. The electron transport to the catalytically active species from the surface can be monitored with this technique.[31] We found that the electron transport is faster in 0.5 M NH_3 solution than in aqueous solution without ammonia substrate (only 0.2 M $NaClO_4$ supporting electrolyte). Moreover, the electron-transporting naphthalene backbone of guest **2** showed a faster electron transport rate (86.6 s^{-1}) than those from guest **1** (46.4 s^{-1}). However, since the catalytic process is slower than the electron transport to the electrode surface, the catalysis is the rate-limiting step. This explains the better performance of guest **1** despite the clearly lower electron transfer rate.

Even though the HG binding is reduced at higher pH, the host remains on the electrode. We could confirm this assumption by the reabsorption of the guests after catalysis more than three times, which we demonstrated in several experiments in both, aqueous and organic solvents (**Figures S38-S39**). Moreover, the reabsorption is not only accessible with the same guests but also with another guest: Guest **1** and guest **2** can be exchanged after catalysis on a sample that was initially functionalized with the other guest, which we demonstrated by absorbing the used

electrodes with fresh exchanged guests. Both reabsorption experiments showed distinctive redox peaks of the related other guest (**Figure S40**).

CONCLUSION

We demonstrated that AO is possible in both organic and aqueous solvents with a host-guest approach. Moreover, we were able to improve upon the HG system we previously reported by incorporating a more stable binding group on the catalyst backbone. The newly designed system displayed increased performance considering different aspects such as stability and faradaic efficiency. This is due to the increased stability of guest **1** at high pH due to the better binding to the host and the earlier onset potential for AO resulting from the different electronic effects on the Ru center from the ligand. Moreover, we found that ammonia oxidation is possible in water as a solvent, without any further supporting electrolyte or buffering system, which demonstrates the increased stability of the system towards higher pH (>11). Different solvents led to different products, with NO_3^- being the sole product in H_2O with up to 98% FE. The recyclability of the host-anchored electrode was demonstrated by the reabsorption (up to 3 times) of new guests without a loss in catalytic activity.

ASSOCIATED CONTENT

All experimental details, synthesis, and compound characterization are given in the SI. This material is available free of charge via the Internet at http://pubs.acs.org.

AUTHOR INFORMATION

Corresponding Author

*S. David Tilley, david.tilley@chem.uzh.ch

University of Zurich, Department of Chemistry, Winterthurerstrasse 190 CH-8057 Zürich,

Present Addresses

[b]Université Paris-Saclay, CEA, CNRS, NIMBE, 91191 Gif-sur-Yvette Cedex, France

Author Contributions

HR carried out syntheses and experimental work and wrote the manuscript. LS helped with electrochemical measurements and writing the manuscript. TM helped with electrochemical measurements. BS measured X-ray crystallography and analyzed crystallographic data. OB helped with X-ray crystallography and analysis. TF optimized and measured ^{14}N NMR. MI performed the DFT calculations and analysis. DT supervised the work. The manuscript was written with input from all authors.

Funding Sources

We gratefully acknowledge the University of Zurich, the University Research Priority Program LightChEC, and the Legerlotz Foundation for funding as well as the Swiss National Supercomputing Centre (CSCS) for computational support under the projects uzh35, financed through the support of the Alfred Werner Legat.

ACKNOWLEDGMENT

We want to thank Nora Grundmann, Prof. Dr. Roger Alberto, Urs Stadler, Daniel Civettini and Prof. Dr. Greta Patzke for their support with gas chromatography measurements.

REFERENCES

(1) Schüth, F.; Palkovits, R.; Schlögl, R.; Su, D. S. Ammonia as a Possible Element in an Energy Infrastructure: Catalysts for Ammonia Decomposition. *Energy Environ. Sci.* **2012**, *5* (4), 6278–6289. https://doi.org/10.1039/C2EE02865D.

(2) Jiao, F.; Xu, B. Electrochemical Ammonia Synthesis and Ammonia Fuel Cells. *Advanced Materials* **2019**, *31* (31), 1805173. https://doi.org/10.1002/adma.201805173.

(3) Qing, G.; Ghazfar, R.; Jackowski, S. T.; Habibzadeh, F.; Ashtiani, M. M.; Chen, C. P.; Smith, M. R.; Hamann, T. W. Recent Advances and Challenges of Electrocatalytic N2Reduction to Ammonia. *Chemical Reviews*. American Chemical Society June 24, 2020, pp 5437–5516. https://doi.org/10.1021/acs.chemrev.9b00659.

(4) Nakajima, K.; Toda, H.; Sakata, K.; Nishibayashi, Y. Ruthenium-Catalysed Oxidative Conversion of Ammonia into Dinitrogen. *Nat Chem* **2019**, *11* (8), 702–709. https://doi.org/10.1038/s41557-019-0293-y.

(5) Habibzadeh, F.; Miller, S. L.; Hamann, T. W.; Smith, M. R. Homogeneous Electrocatalytic Oxidation of Ammonia to N $_2$ under Mild Conditions. *Proceedings of the National Academy of Sciences* **2019**, *116* (8), 2849–2853. https://doi.org/10.1073/pnas.1813368116.

(6) Dunn, P. L.; Johnson, S. I.; Kaminsky, W.; Bullock, R. M. Diversion of Catalytic C–N Bond Formation to Catalytic Oxidation of NH $_3$ through Modification of the Hydrogen Atom Abstractor. *J Am Chem Soc* **2020**, *142* (7), 3361–3365. https://doi.org/10.1021/jacs.9b13706.

(7) Dunn, P. L.; Cook, B. J.; Johnson, S. I.; Appel, A. M.; Bullock, R. M. Oxidation of Ammonia with Molecular Complexes. *J Am Chem Soc* **2020**, *142* (42), 17845–17858. https://doi.org/10.1021/jacs.0c08269.

(8) Holub, J.; Vereshchuk, N.; Sánchez-Baygual, F.-J.; Gil-Sepulcre, M.; Benet-Buchholz, J.; Llobet, A. Synthesis, Structure, and Ammonia Oxidation Catalytic Activity of Ru-NH $_3$ Complexes Containing Multidentate Polypyridyl Ligands. *Inorg Chem* **2021**, *60* (18), 13929–13940. https://doi.org/10.1021/acs.inorgchem.1c01528.

(9) Zott, M. D.; Peters, J. C. Enhanced Ammonia Oxidation Catalysis by a Low-Spin Iron Complex Featuring *Cis* Coordination Sites. *J Am Chem Soc* **2021**, *143* (20), 7612–7616. https://doi.org/10.1021/jacs.1c02232.

(10) Stephens, D. N.; Szilagyi, R. K.; Roehling, P. N.; Arulsamy, N.; Mock, M. T. Catalytic Ammonia Oxidation to Dinitrogen by a Nickel Complex. *Angewandte Chemie* **2023**, *135* (1). https://doi.org/10.1002/ange.202213462.

(11) Zott, M. D.; Garrido-Barros, P.; Peters, J. C. Electrocatalytic Ammonia Oxidation Mediated by a Polypyridyl Iron Catalyst. *ACS Catal* **2019**, *9* (11), 10101–10108. https://doi.org/10.1021/acscatal.9b03499.

(12) Li, Y.; Chen, J.-Y.; Miao, Q.; Yu, X.; Feng, L.; Liao, R.-Z.; Ye, S.; Tung, C.-H.; Wang, W. A Parent Iron Amido Complex in Catalysis of Ammonia Oxidation. *J Am Chem Soc* **2022**, *144* (10), 4365–4375. https://doi.org/10.1021/jacs.1c08609.

(13) Jabłońska, M.; Palkovits, R. Copper Based Catalysts for the Selective Ammonia Oxidation into Nitrogen and Water Vapour—Recent Trends and Open Challenges. *Appl Catal B* **2016**, *181*, 332–351. https://doi.org/10.1016/j.apcatb.2015.07.017.

(14) Ahmed, M. E.; Raghibi Boroujeni, M.; Ghosh, P.; Greene, C.; Kundu, S.; Bertke, J. A.; Warren, T. H. Electrocatalytic Ammonia Oxidation by a Low-Coordinate Copper Complex. *J Am Chem Soc* **2022**, *144* (46), 21136–21145. https://doi.org/10.1021/jacs.2c07977.

(15) Toda, H.; Kuroki, K.; Kanega, R.; Kuriyama, S.; Nakajima, K.; Himeda, Y.; Sakata, K.; Nishibayashi, Y. Manganese-Catalyzed Ammonia Oxidation into Dinitrogen under Chemical or Electrochemical Conditions**. *Chempluschem* **2021**, *86* (11), 1511–1516. https://doi.org/10.1002/cplu.202100349.

(16) Liu, H.-Y.; Lant, H. M. C.; Troiano, J. L.; Hu, G.; Mercado, B. Q.; Crabtree, R. H.; Brudvig, G. W. Electrocatalytic, Homogeneous Ammonia Oxidation in Water to Nitrate and Nitrite with a Copper Complex. *J Am Chem Soc* **2022**, *144* (19), 8449–8453. https://doi.org/10.1021/jacs.2c01788.

(17) Grand view research. *Nitric Acid Market Size, Share & Trends Analysis Report By Application (Fertilizers, Nitrobenzene, Adipic Acid, Toluene Di-Isocyanate, Nitoroclorobenzene), By Region, And Segment Forecasts, 2023 - 2030*; 2019.

(18) Lim, J.; Fernández, C. A.; Lee, S. W.; Hatzell, M. C. Ammonia and Nitric Acid Demands for Fertilizer Use in 2050. *ACS Energy Lett* **2021**, *6* (10), 3676–3685. https://doi.org/10.1021/acsenergylett.1c01614.

(19) Beiler, A. M.; Denisiuk, A.; Holub, J.; Sánchez-Baygual, F.-J.; Gil-Sepulcre, M.; Ertem, M. Z.; Moonshiram, D.; Piccioni, A.; Llobet, A. Heterogeneous Electrochemical Ammonia Oxidation with a Ru-Bda Oligomer Anchored on Graphitic Electrodes via CH−π Interactions. *ACS Energy Lett* **2022**, 172–178. https://doi.org/10.1021/acsenergylett.2c02483.

(20) Sévery, L.; Szczerbiński, J.; Taskin, M.; Tuncay, I.; Brandalise Nunes, F.; Cignarella, C.; Tocci, G.; Blacque, O.; Osterwalder, J.; Zenobi, R.; Iannuzzi, M.; Tilley, S. D. Immobilization of Molecular Catalysts on Electrode Surfaces Using Host–Guest Interactions. *Nat Chem* **2021**, *13* (6), 523–529. https://doi.org/10.1038/s41557-021-00652-y.

(21) Vícha, R.; Rouchal, M.; Kozubková, Z.; Kuřitka, I.; Marek, R.; Branná, P.; Čmelík, R. Novel Adamantane-Bearing Anilines and Properties of Their Supramolecular Complexes with β-Cyclodextrin. *Supramol Chem* **2011**, *23* (10), 663–677. https://doi.org/10.1080/10610278.2011.593628.

(22) Granadero, D.; Bordello, J.; Pérez-Alvite, M. J.; Novo, M.; Al-Soufi, W. Host-Guest Complexation Studied by Fluorescence Correlation Spectroscopy: Adamantane–Cyclodextrin Inclusion. *Int J Mol Sci* **2010**, *11* (1), 173–188. https://doi.org/10.3390/ijms11010173.

(23) Wang, J.-W.; Yu, K.-X.; Ji, X.-Y.; Bai, H.; Zhang, W.-H.; Hu, X.; Tang, G. Structural Insights into the Host–Guest Complexation between β-Cyclodextrin and Bio-Conjugatable Adamantane Derivatives. *Molecules* **2021**, *26* (9), 2412. https://doi.org/10.3390/molecules26092412.

(24) T. Pessine, F. B.; Calderini, A.; L., G. Review: Cyclodextrin Inclusion Complexes Probed by NMR Techniques. In *Magnetic Resonance Spectroscopy*; InTech, 2012. https://doi.org/10.5772/32029.

(25) Thordarson, P. Determining Association Constants from Titration Experiments in Supramolecular Chemistry. *Chem. Soc. Rev.* **2011**, *40* (3), 1305–1323. https://doi.org/10.1039/C0CS00062K.

(26) *http://supramolecular.org*.

(27) Szente, L.; Singhal, A.; Domokos, A.; Song, B. Cyclodextrins: Assessing the Impact of Cavity Size, Occupancy, and Substitutions on Cytotoxicity and Cholesterol Homeostasis. *Molecules* **2018**, *23* (5), 1228. https://doi.org/10.3390/molecules23051228.

(28) Sandilya, A. A.; Natarajan, U.; Priya, M. H. Molecular View into the Cyclodextrin Cavity: Structure and Hydration. *ACS Omega* **2020**, *5* (40), 25655–25667. https://doi.org/10.1021/acsomega.0c02760.

(29) Brynn Hibbert, D.; Thordarson, P. The Death of the Job Plot, Transparency, Open Science and Online Tools, Uncertainty Estimation Methods and Other Developments in Supramolecular Chemistry Data Analysis. *Chemical Communications* **2016**, *52* (87), 12792–12805. https://doi.org/10.1039/C6CC03888C.

(30) Kühne, T. D.; Iannuzzi, M.; Del Ben, M.; Rybkin, V. V.; Seewald, P.; Stein, F.; Laino, T.; Khaliullin, R. Z.; Schütt, O.; Schiffmann, F.; Golze, D.; Wilhelm, J.; Chulkov, S.; Bani-Hashemian, M. H.; Weber, V.; Borštnik, U.; Taillefumier, M.; Jakobovits, A. S.; Lazzaro, A.; Pabst, H.; Müller, T.; Schade, R.; Guidon, M.; Andermatt, S.; Holmberg, N.; Schenter, G. K.; Hehn, A.; Bussy, A.; Belleflamme, F.; Tabacchi, G.; Glöß, A.; Lass, M.; Bethune, I.; Mundy, C. J.; Plessl, C.; Watkins, M.; VandeVondele, J.; Krack, M.; Hutter, J. CP2K: An Electronic Structure and Molecular Dynamics Software Package - Quickstep: Efficient and Accurate Electronic Structure Calculations. *J Chem Phys* **2020**, *152* (19). https://doi.org/10.1063/5.0007045.

(31) Chidsey, C. E. D. Free Energy and Temperature Dependence of Electron Transfer at the Metal-Electrolyte Interface. *Science (1979)* **1991**, *251* (4996), 919–922. https://doi.org/10.1126/science.251.4996.919.

.

Supporting Information

Electrocatalytic Ammonia Oxidation with a Tailored Molecular Catalyst Heterogenized via Surface Host-Guest Complexation

Helena Roithmeyer[a], Laurent Sévery[a,b], Thomas Moehl[a], Bernhard Spingler[a], Olivier Blacque[a], Thomas Fox[a], Marcella Iannuzzi[a] and S. David Tilley[a]*

[a]Department of Chemistry, University of Zürich, Winterthurerstrasse 190, 8057, Zurich, Switzerland

Table of Contents

General Information & Instrumentation

The bis-phosphonated β-CD and the [Ru(tpnp)(bpy-NMe_2)(Cl)](PF_6) (guest **2**) were synthesized and characterized as published before.[1] All reagents were purchased from Sigma Aldrich or Chemie Brunschwig, except for 4,4'-bis(dimethylamino)-2,2'-bipyridine (99%, Hetcat, Switzerland). All solvents were used in the analytical grade. Water was used in the MiliQ grade. Dry solvents were handled under N_2 inert atmosphere (Schlenk line or glovebox). 0.5M NH_3 in THF was purchased from Sigma Aldrich. Fluorine-doped tin oxide (FTO) glass plates were *Pilkington NSG TEC 15* (2.2 mm, 12–15 Ω/sq). Indium tin oxide (ITO) particles and proprietary nanopowder dispersant were purchased from *US Research Nanomaterials Inc.*, Houston, TX, USA.

NMR spectroscopy

All spectra were acquired on a 400 or 500 MHz Bruker Avance spectrometer. All spectra were referenced according to their residual solvent signals and processed with Mnova.

Mass spectrometry

Mass spectra were taken on a Thermo DFS High-resolution mass analyzer (GC)MS equipped with electron- and chemical-ionization (EI and CI), direct chemical ionization (DCI), gas chromatograph (GC), and autosampler incl. headspace sampling and automatic derivatization.

UV-Vis spectroscopy

The measurements were conducted on a SHIMADZU UV-3600 Plus Spectrophotometer. The related solvent or mITO- electrode was used as a reference/ blank.

X-ray crystallography

Crystallographic data were collected on a Rigaku Oxford Diffraction XtaLAB Synergy-S dual source diffractometer fitted with a Rigaku HyPix-6000HE HPC (Hybrid Photon Counting) detector, Cu and Mo PhotonJet microfocus X-ray sources, and an Oxford Cryosystems Cryostream 800 cooler maintaining a temperature of 160.0(1) K. Suitable crystals were covered with oil (Infineum V8512, formerly known as Paratone N), placed on a nylon loop that is mounted on a CrystalCap Magnetic™ pin (Hampton Research) and immediately transferred to the diffractometer. The program suite *CrysAlis^{Pro}* was used for data collection, numerical and multi-scan absorption correction as well, as data reduction.[2] The structures were solved with the dual-space algorithm using *SHELXT*[3] and were refined by full-matrix least-squares methods on F^2 with *SHELXL-2018*[4] using the *Olex2* GUI.[5] CCDC 2244246-2244248 contain the supplementary crystallographic data for this paper. These data are provided free of charge by The Cambridge Crystallographic Data Centre *via* www.ccdc.cam.ac.uk/structures. The graphical output was produced with the help of the program *Mercury*.[6] **Guest 1:** The adamantyl group is disordered in a ratio of 53: 47. Ill-defined electron density of some co-solvents had to be treated with the *SQUEEZE* procedure within *Platon*.[7]

CCDC 2244246-2244248 contain the supplementary crystallographic data for this paper. These data are provided free of charge by The Cambridge Crystallographic Data Centre *via* www.ccdc.cam.ac.uk/structures.

Electrochemistry

Electrochemical measurements were conducted on a BioLogic SP-150 potentiostat using a three-electrode set-up. FTO with spin-coated mITO (see experimental) and functionalized host (H) and guest (G) served as the working electrode. A platinum wire was used as the counter electrode, and an AgCl wire in 0.1 M $TBAPF_6$ in THF or MeOH for the measurements in organic solvents, or 0.2 M $NaClO_4$ in H_2O for the measurements in aqueous medium was used as a reference electrode. The pH of the aqueous solutions was measured with a pH meter. As a reference physisorbed guest on the mITO electrode without the host was measured.

Experimental

Synthesis and characterization

1-adamantane carboxaldehyde:

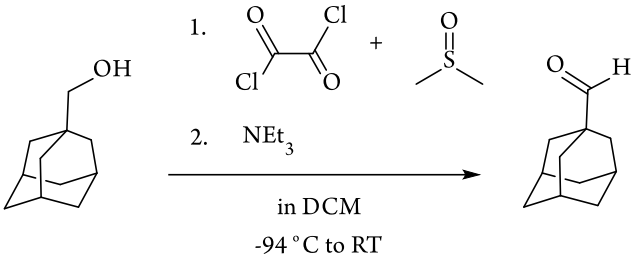

Scheme S 1: Synthetic route to 1- adamantane carboxaldehyde.

1-Adamantanecarboxaldehyde was synthesized according to literature[8]: 5.57 mL (64.96 mmol, 1.2 equiv.) oxalyl chloride was added to 60 mL DCM cooled to -94°C (acetone/N_2 bath) and 9.23 mL (129.9 mmol, 2.4 equiv.) DMSO in 30 mL DCM were added slowly over 30 min to the mixture and stirred for 15 min before 1 equivalent of 1-adamantanemethanol in 90 mL DCM was added over 20 min and stirred for another 15 min. Afterwards, 30 mL (216.5 mmol, 4 equiv.) NEt_3 was added and stirred for 2.5 h at 0°C. The reaction was quenched by adding 100 mL H_2O, and the water phase was extracted twice with DCM. The organic layers were extracted with water, brine, and water again and dried over Mg_2SO_4, filtered, and evaporated to give 8.15 g (92%) as a white powder. The product was used without further purification for the next step.

^{1}H NMR (400 MHz, $CDCl_3$) δ 9.31 (s, 1H, CO**H),** 2.07 – 1.58 (m, 15H, Adamantane-H)

^{13}C NMR (101 MHz, $CDCl_3$) δ 206.01 (s, 1C, **C**OH**),** 45.80, 36.58, 35.86, 27.37. (adamantane-C)

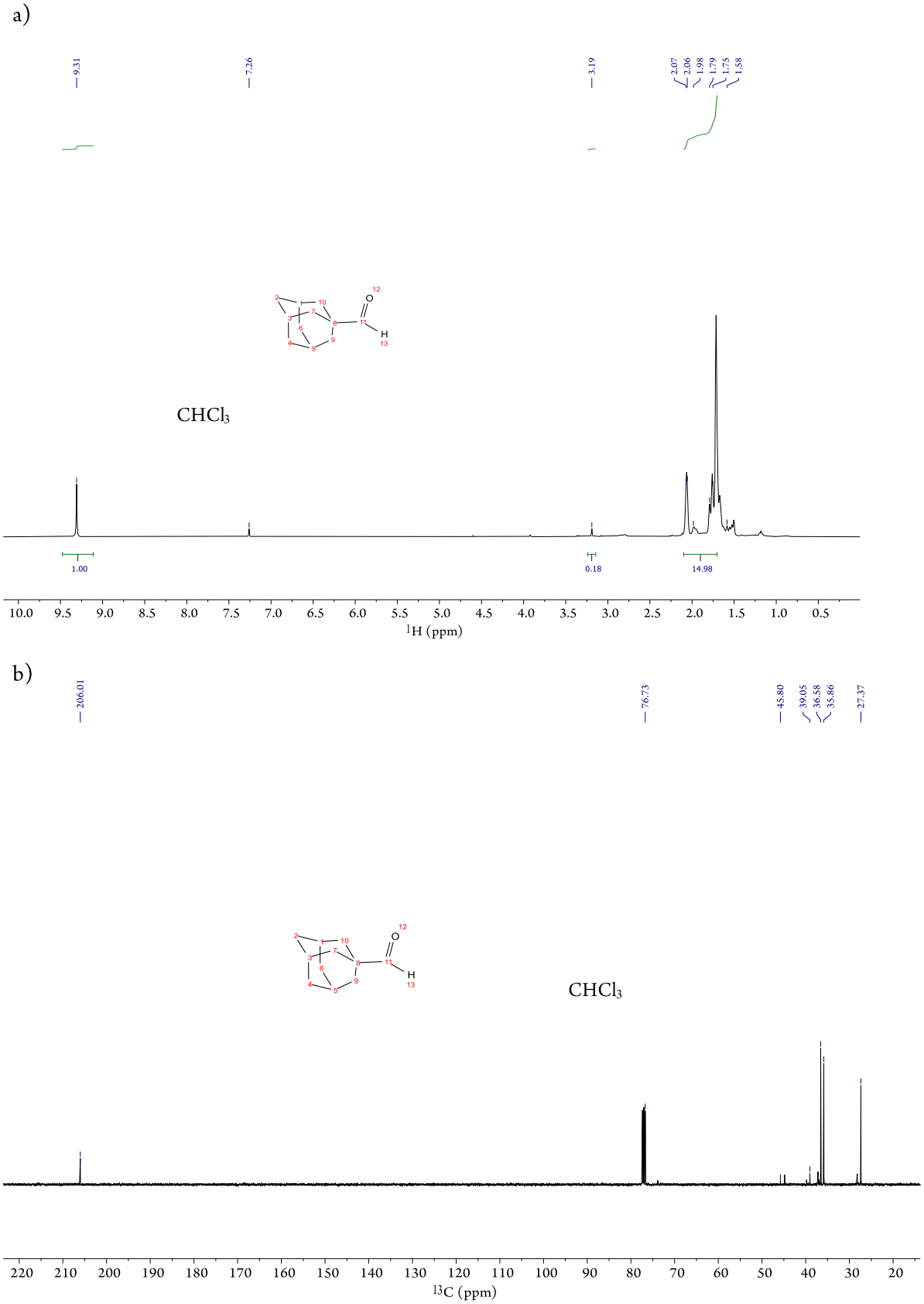

Figure S 1: a) ^{1}H and b) ^{13}C NMR of 1-adamantane carboxaldehyde in $CDCl_3$.

Terpyridine adamantane (tpada)

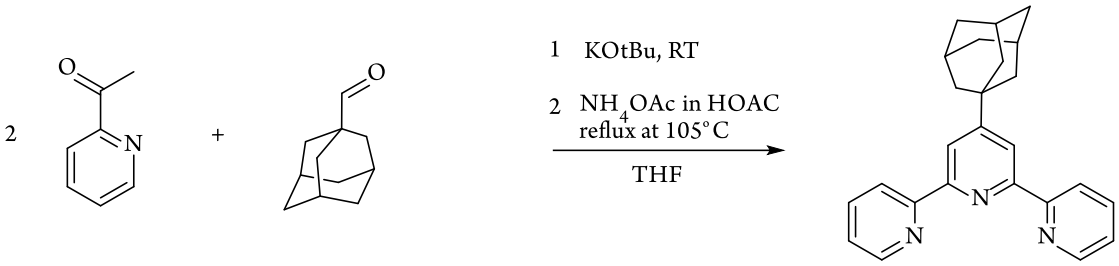

Scheme S 2: Synthetic route to terpyridine adamantane.

Two equivalents of 2-acetylpyridine (6.54 mL, 0.058 mol) were added to a mixture of 2 equiv. KOtBu (6.51 g, 0.058 mol) in 160 mL THF and 1. equiv. of 1-adamantane carboxaldehyde (4.79 g, 0.029 mol) was added, and the red mixture was stirred for 4 h at RT. Afterwards, 22.35 g (0.29 mol) ammonium acetate dissolved in 100 ml glacial acetic acid was added, and the mixture was refluxed (105 ºC) for 16h. The solvent was evaporated to give a brown-yellow residue which was neutralized with saturated $NaHCO_3$ solution to a pH 6-7. Afterwards, diethyl ether was added. The water phase was washed with diethyl ether to give a yellow mixture in Et_2O. The organic layer was washed three times with (each 100 mL) H_2O. The organic layers were combined, dried over Mg_2SO_4, filtered, and evaporated to give a yellow-brown residue.[9] The mixture was packed on an Al_2O_3 column in Et_2O/hexane (1:1.5). A light yellow eluent was obtained, which was evaporated. The residue yellow powder was washed with hexane and dried to give a light yellow microcrystalline powder (27%).

^{1}H NMR (400 MHz, $CDCl_3$) δ 8.68 (dd, *J* = 8.0, 8.0 Hz, 4H, 3;15;6;18), 8.49 (s, 2H, 7;11), 7.92 – 7.73 (m, 2H, *J* = 8.0, 1;17), 7.32 (d, *J* = 13.6 Hz, 2H, 2;16), 2.17 – 1.82 (m, *J* = 4 Hz, 15H, adamantane-H, 19 – 28).

^{13}C NMR (101 MHz, $CDCl_3$) δ 162.3 (12), 156.8, 155.4 (8;10), 149.1 (3;15), 137.0 (1;17), 123.7 (2;16), 121.5 (6;18), 118.0 (7;11), 42.6 (27;28;25), 37.1; 36.8 (20;22;24;26), 28.9 (19;21;23).

HRMS ESI$^+$: *m/z* $[M+H]^+$ $C_{25}H_{26}N_3^+$ calc. 368.2121 found 368.2120

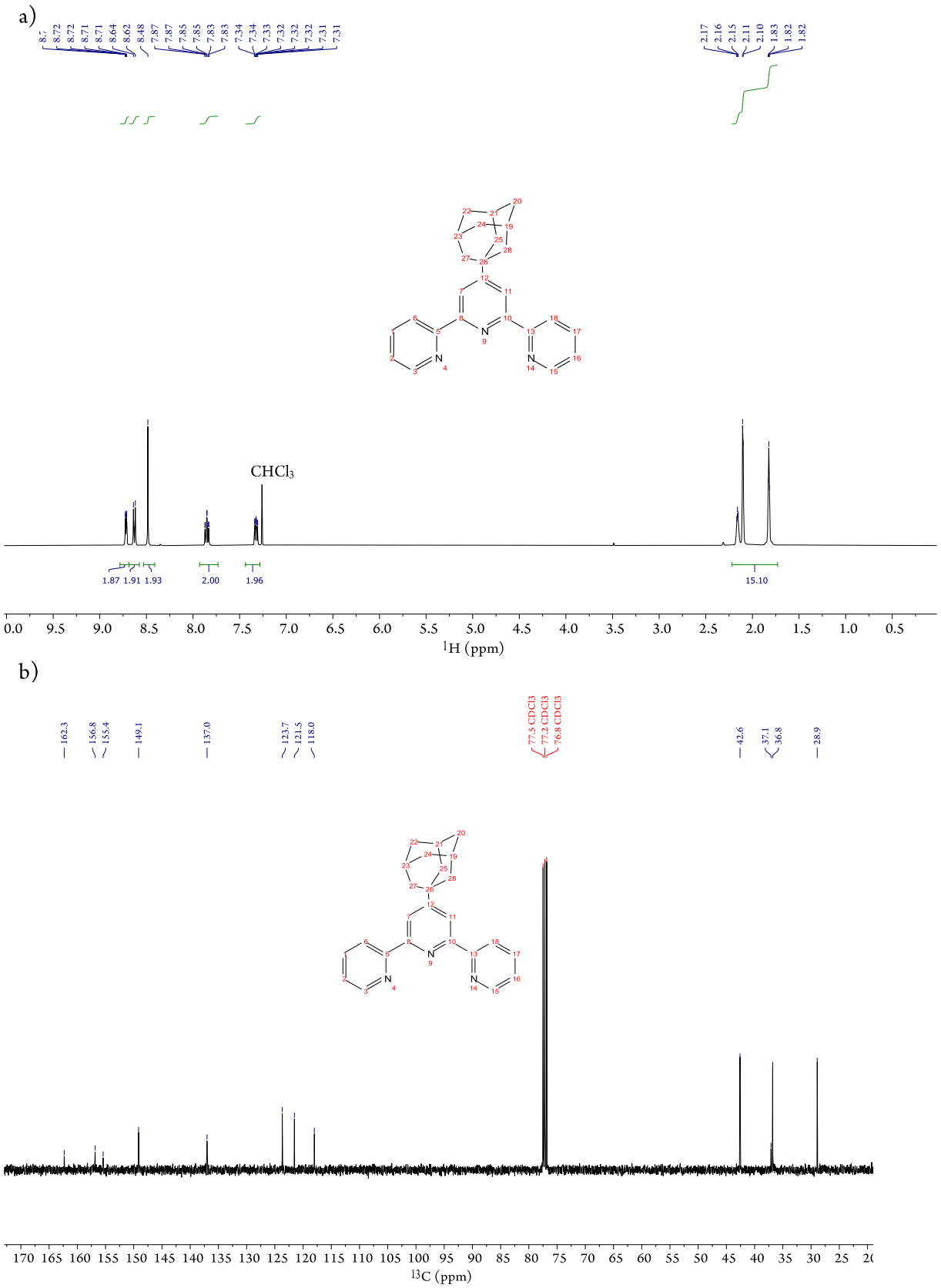

Figure S 2: a) ^{1}H and b) ^{13}C NMR of terpyridine-adamantane (tpada) in $CDCl_3$.

[(Ru(bpy-NMe$_2$)(tpada)(Cl)](PF$_6$)- guest 1

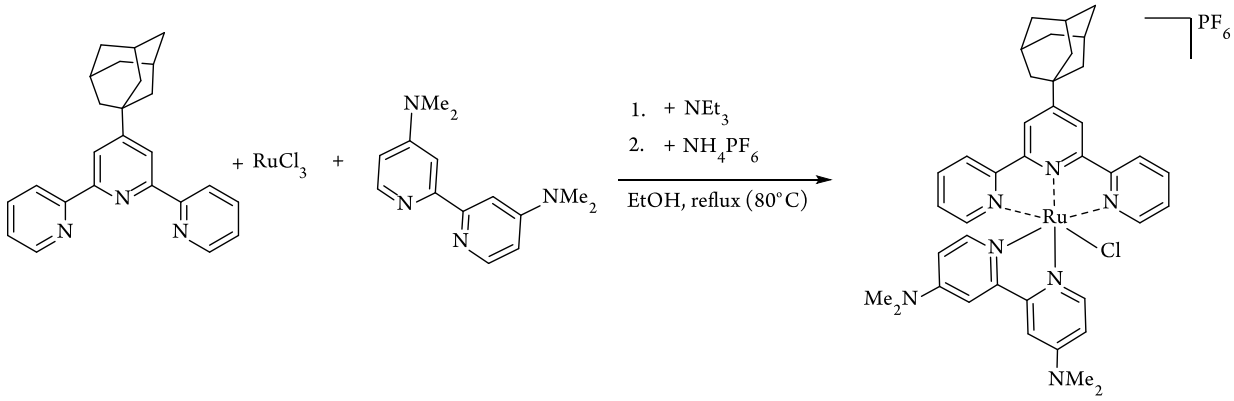

Scheme S 3: Synthetic route to [(Ru(bpy-NMe$_2$)(tpada)(Cl)](PF$_6$) guest **1.**

203.7 mg (0.55 mmol, 1 equiv.) terpyridine adamantane and 287.4 mg (1.39 mmol, 2.5 equiv.) $RuCl_3$ hydrate (38-42%) were refluxed in 50 mL EtOH for 3h. Afterwards the mixture was filtered to give a brown filter cake, which was washed with EtOH, pentane, and diethyl ether. The powder was dried on air to give 376 mg (47%) tpadaRuCl$_3$.

171.2 mg (0.30 mmol, 1 equiv.) tpadaRuCl$_3$, 72.2 mg (0.30 mmol, 1 equiv.) (bpy-NMe$_2$) and 0.2 ml (1.43 mol) NEt_3 were dissolved in 60 mL EtOH and refluxed at 80°C for 3.5 h. Afterwards, the mixture was cooled to RT, and an excess (spatula tip) of NH_4PF_6 was added and stirred for another 30 min. A dark purple precipitate formed while cooling to RT which was filtered off and purified with column chromatography (DCM: MeOH 98:2 to 95:5) and dried under vacuum to give 192.2 mg (74%) [Ru(bpy-NMe$_2$)(Cl)(tpada)](PF$_6$) as a dark purple crystalline powder.

The synthesis in a one-pot reaction with the same purification led to 45% yield.

It was noteworthy that after a while the compound showed poor solubility in chlorinated solvents, and high solubility in acetone or MeOH.

^{1}H NMR (500 MHz, acetone-*d*$_6$) δ 9.73 – 9.72 (m, *J* = 5.0 Hz ,1H, 39), 8.71 – 8.70 (m, *J* = 5.0 Hz, 4H, 2,7,11,16), 7.94 – 7.90 (m, *J* = 10.0 Hz, 5H,1,3,15,17,42), 7.66 – 7.65 (d, *J* = 5.0, 1H, 36), 7.43 – 7.40 (m, *J* = 5.0, 10 Hz, 2H, 6,18), 7.29 – 7.27 (m, *J* = 10.0 Hz, 1H, 32), 6.63 – 6.61 (m, *J* = 10.0 Hz, 1H, 33), 6.24 – 6.22 (dd, *J* = 10.0 Hz, 1H, 40), 3.37 (s, 6H, N-CH$_3$, 44,45), 3.00 (s, 6H, N-CH$_3$, 47,48), 2.29 – 2.24 (m, *J* = 5.0 Hz, 9H, adamantane-H), 1.93 – 1.92 (m, *J* = 5.0 Hz, 6H, adamantane-H)

^{13}C NMR (126 MHz, acetone-*d*$_6$) δ 160.72; 159.74 (bpy-C, 35, 37), 158.88 (terpyridine-C, 12), 157.15; 156.90 (bpy-C, 31, 41), 155.56; 154.48 (terpyridine-C, 5,8,10,13), 152.82 (terpyridine-C, 1,17), 151.85 (bpy-C, 39), 150.19 (bpy-C, 33), 136.44 (terpyridine-C, 3,15), 127.65 (terpyridine- C, 6,18), 123.82; 119.90 (terpyridine-C, 2,7,11,16) 109.98; 109.73 (bpy-C, 32, 40), 106.16;105.87 (bpy-C, 36, 42), 43.15 (adamantane-C), 39.82; 39.44 (N-CH$_3$, 44,45,47,48), 38.24 (26), 37.14 (adamantane-C).

^{31}P NMR (162 MHz, CD_2Cl_2) δ -135.59 – -153.20 (sept, PF_6)

HRMS ESI$^+$: *m/z* [M-PF$_6$]$^+$ $C_{39}H_{43}ClN_7Ru$ calc. 746.2306 found 746.2305

Single crystals were obtained by diffusion of diethyl ether into an acetone/MeOH mixture of the compound.

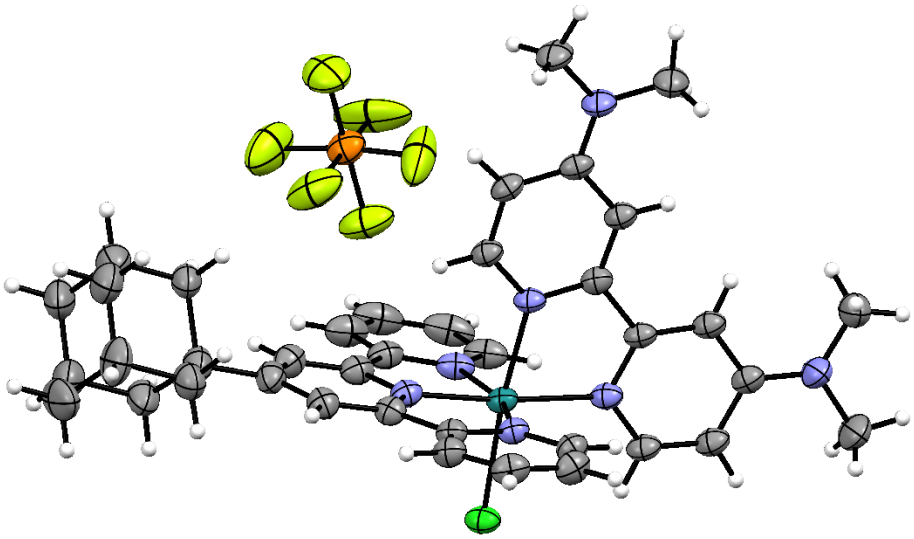

Figure S 3: Ellipsoidal representation of guest **1** Ellipsoids are drawn at 50% probability; the disordered parts of the hexafluorophosphate anion and the adamantly group, as well as the co-solvent diethyl ether, have been omitted for clarity.

Table S 1: Crystal Data and Structure Refinement for Guest **1**

Empirical formula	$C_{43}H_{53}ClF_6N_7OPRu$
Formula weight	965.41
Crystal system	Triclinic
Space group	$P\bar{1}$
a [Å]	8.78410(15)
b [Å]	16.0523(3)
c [Å]	17.42786(20)
α [°]	83.3399(11)
β [°]	80.0155(12)
γ [°]	86.3137(14)
Volume [$Å^3$]	2401.41(7)
Z	2
Density (calculated) [Mg/m^3]	1.335
Temperature [K]	159.99(11)
Wavelength [Å]	1.54184
Absorption coefficient [mm^{-1}]	4.000
F(000)	996
Crystal size [mm^3]	0.086 x 0.039 x 0.01
Crystal description	red plate
Theta range for data collection [°]	2.589 to 80.231
Index ranges	-11<=h<=11, -20<=k<=20, -18<=l<=22
Reflections collected	39743
Independent reflections	10195 [R(int) = 0.0402]
Reflections observed	9186
Criterion for observation	I > 2 σ (I)
Completeness to theta	99.6 % to 67.684°
Absorption correction	Gaussian
Max. and min. transmission	1.000 and 0.745
Data / restraints / parameters	10195 / 0 / 666
Goodness-of-fit on F^2	1.120
Final R indices [I > 2 σ (I)]	R1 = 0.0403, wR2 = 0.1091
R indices (all data)	R1 = 0.0445, wR2 = 0.1112
Largest diff. peak and hole [$e.Å^{-3}$]	0.813 and -1.104

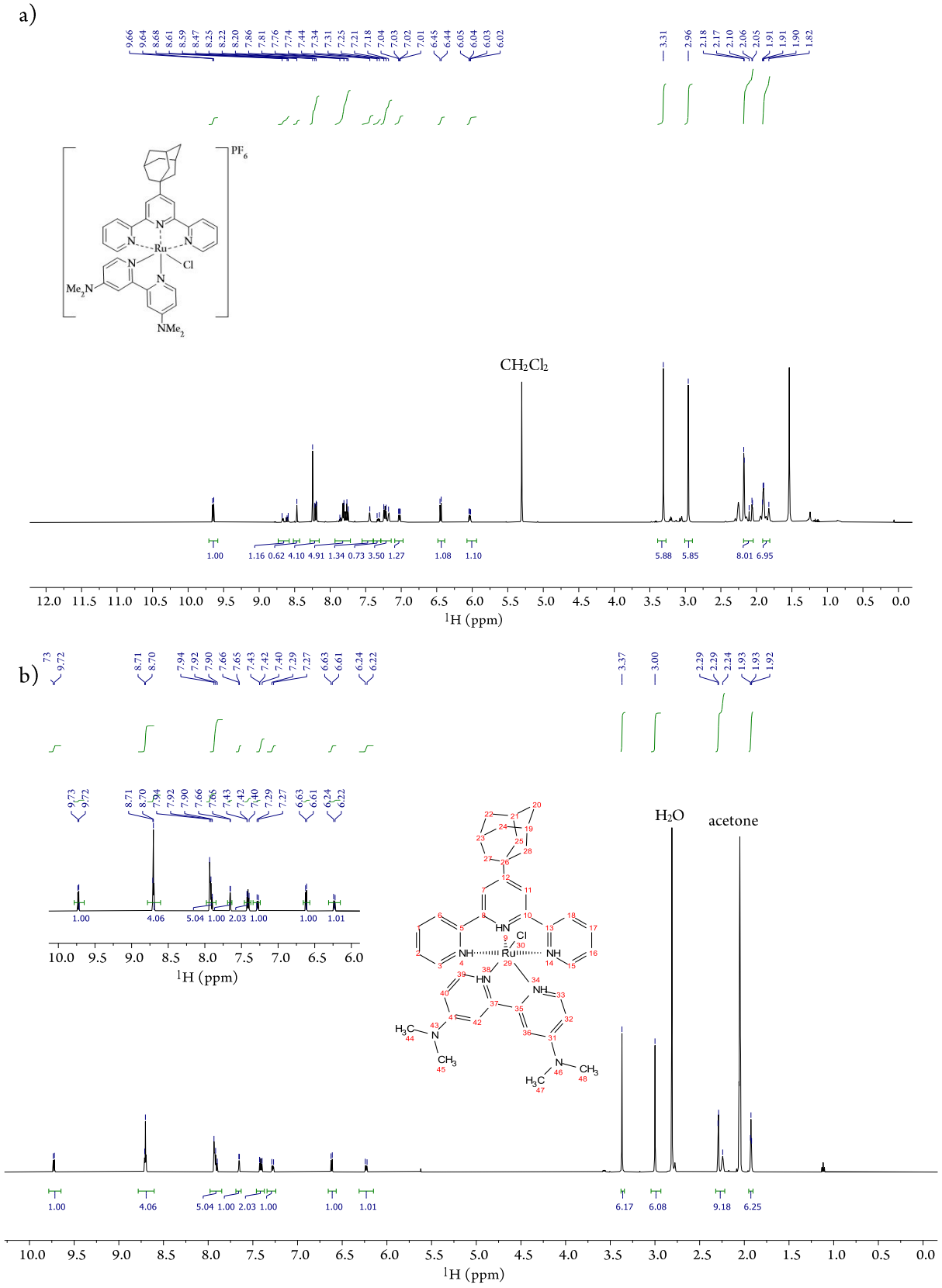

Figure S 4: a) ^{1}H in CD_2Cl_2 and b) ^{1}H NMR in acetone-d_6.

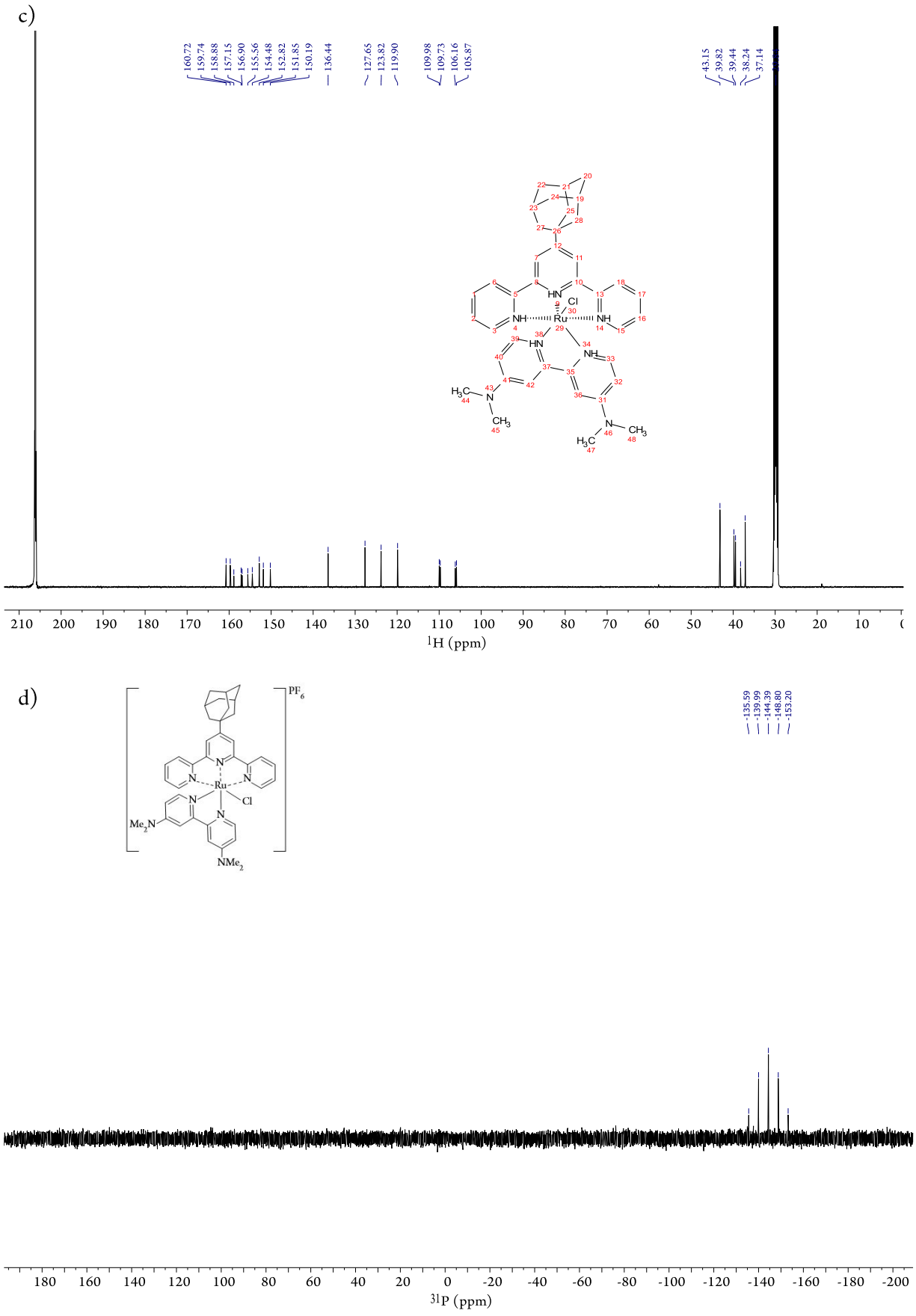

Figure S 5: c) ^{13}C NMR in acetone-d_6 d) ^{31}P NMR in CD_2Cl_2 of [(Ru(bpy-NMe_2)(tpada)(Cl)](PF_6) **1**.

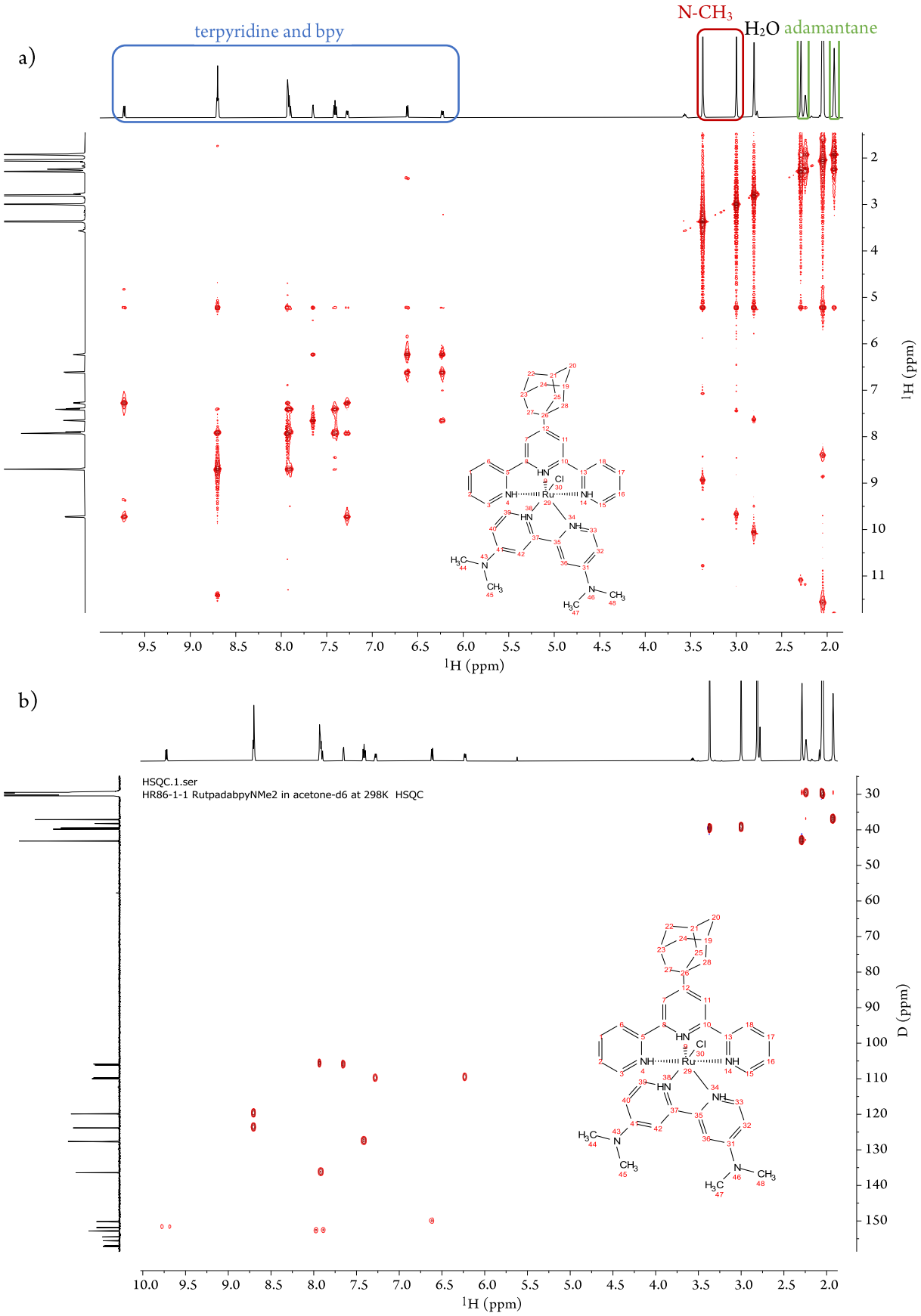

Figure S 6: a) COSY (^{1}H-^{1}H) and b) HSQC (^{13}C-^{1}H) NMR of [(Ru(bpy-NMe$_2$)(tpada)(Cl)](PF$_6$) **1** in acetone-d_6 at 298K.

The intermediate tpadaRuCl$_3$ can be isolated and was crystallized by vapor diffusion from Et$_2$O into an acetone mixture.

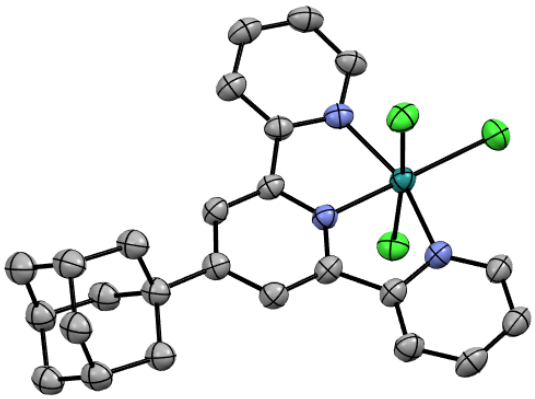

Figure S 7: Crystal structure of [RuCl$_3$(tpada)]. Solvent molecules are omitted for clarity. The adamantane ligand is disordered over two sets of positions with site-occupancy factors of 0.413(4) and 0.587(4). The main species co-crystallized with solvent molecules of acetone in a ratio 1:1.

Table S 2: Crystal Data of [RuCl$_3$(tpada)]

Empirical formula	$C_{28}H_{31}Cl_3N_3ORu$
Formula weight	632.98
Temperature/K	160(1)
Crystal system	orthorhombic
Space group	$P2_12_12_1$
a/Å	9.9547(1)
b/Å	12.7474(1)
c/Å	20.8877(2)
α/°	90
β/°	90
γ/°	90
Volume/Å^3	2650.58(4)
Z	4
Density (calculated) [Mg/m^3]	1.586
μ/mm-1	7.784
F(000)	1292.0
Crystal size/mm^3	0.1 × 0.07 × 0.02
Radiation	Cu Kα (λ = 1.54184)
2Θ range for data collection/°	8.126 to 148.946
Index ranges	-12 ≤ h ≤ 11, -13 ≤ k ≤ 15, -26 ≤ l ≤ 24
Reflections collected	29725
Independent reflections	5405 [Rint = 0.0309, Rsigma = 0.0211]
Data/restraints/parameters	5405/936/409
Goodness-of-fit on F^2	1.047
Final R indexes [I>=2σ (I)]	R1 = 0.0279, wR2 = 0.0705
Final R indexes [all data]	R1 = 0.0301, wR2 = 0.0717
Largest diff. peak/hole / [e Å^{-3}]	0.93/-0.51
Flack parameter	-0.037(4)

[Ru(bpy)(Cl)(tpada)](PF$_6$)- guest 3

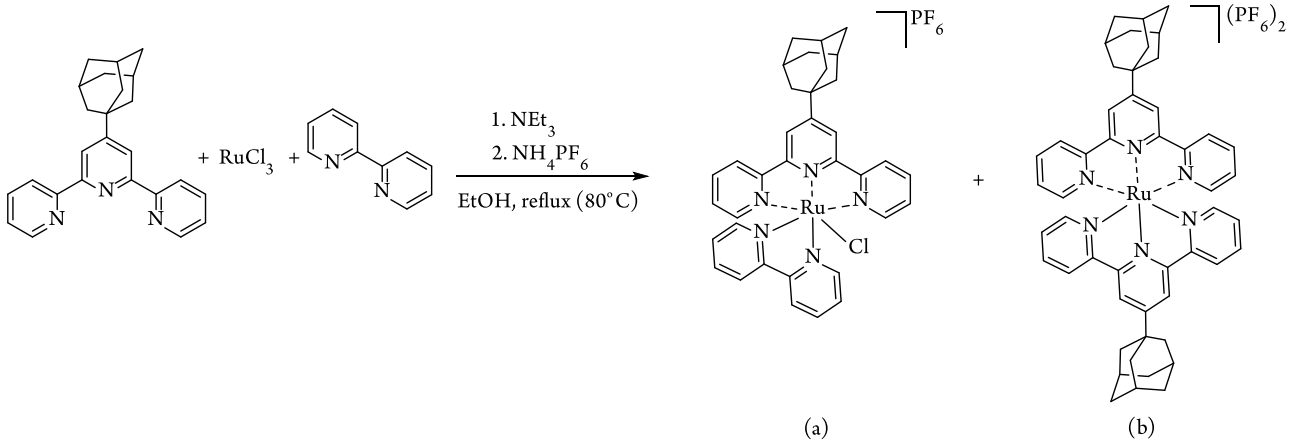

Scheme 4: Synthetic route to **3** [Ru(bpy)(Cl)(tpada)](PF$_6$).

Terpyridine adamantane (79.1 mg, 0.22 mmol) and 1 equiv. $RuCl_3$ anhydrous (44.65 mg, 0.22 mmol) and 1 equiv. bipyridine (33.62 mg, 0.22 mmol) were dissolved in 60 mL EtOH. Afterwards 90 µL NEt_3 (0.64 mmol, 3 equiv.) were added and refluxed at 80°C for 3h. The dark red-purple mixture was cooled to RT, and an excess (spatula tip) of NH_4PF_6 was added and stirred for 30 min. The mixture was filtered, evaporated, and purified with column chromatography (DCM: MeOH 95:5 to 90:10). Two products were isolated: [Ru(bpy)(Cl)(tpada)](PF$_6$) dark purple powder 62.1 mg (39%) and [Ru(tpada)$_2$](PF$_6$)$_2$ intense red powder.

Characterization of a:[Ru(bpy)(Cl)(tpada)](PF$_6$)

^{1}H NMR (400 MHz, $CDCl_3$) δ 10.34 – 10.32 (d, *J* = 8.0 Hz, 1H), 8.74 – 8.63 (m, *J* = 8.0; 8.0; 8 Hz 5H), 8.56 (d, *J* = 8.0 Hz, 1H), 8.49 (s, 2H), 8.42 (d, *J* = 8.0 Hz, 1H), 8.31 – 8.25 (s, d, *J* = 8.0 Hz 5H), 8.21– 8.17 (t, *J* = 8.0 Hz, 1H), 7.89 – 7.76 (m, *J* = 8.0, 4.0, 12 Hz, 6H), 7.66 – 7.59 (m, *J* = 8.0, 12 Hz, 3H), 7.36 – 7.31 (m, *J* = 8.0 Hz, 3H), 7.21 (m, *J* = 12.0, 4.0 Hz, 2H), 7.06 – 7.03 (t, *J* = 4.0 Hz, 1H), 2.11 (d, *J* = 4.0 Hz, 4H, adamantane), 1.90; 1.83 (m, *J* = 4.0, 4.0 Hz, 12H (6+6), adamantane).

^{13}C NMR (126 MHz, $CDCl_3$) δ 162.52, 158.89, 158.19, 157.12, 156.28, 155.51, 152.79, 151.82, 147.52, 136.40, 135.71, 126.98, 126.43, 123.40, 123.13, 119.52, 42.55, 37.46, 36.32, 28.61.

HRMS ESI$^+$: $[M\text{-}PF_6]^+$ $C_{35}H_{33}ClN_5Ru$ calc. 660.1462 found 660.1457

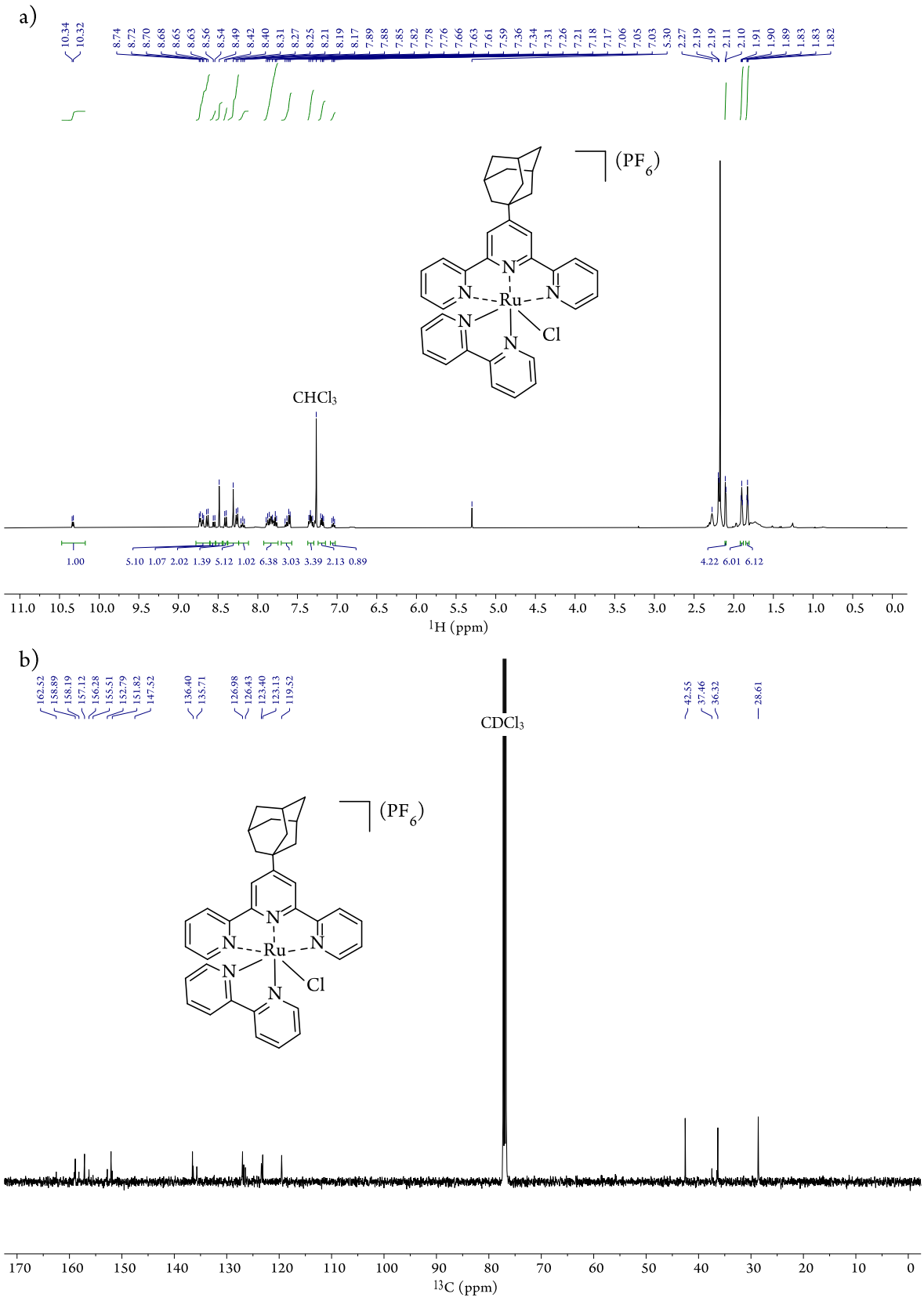

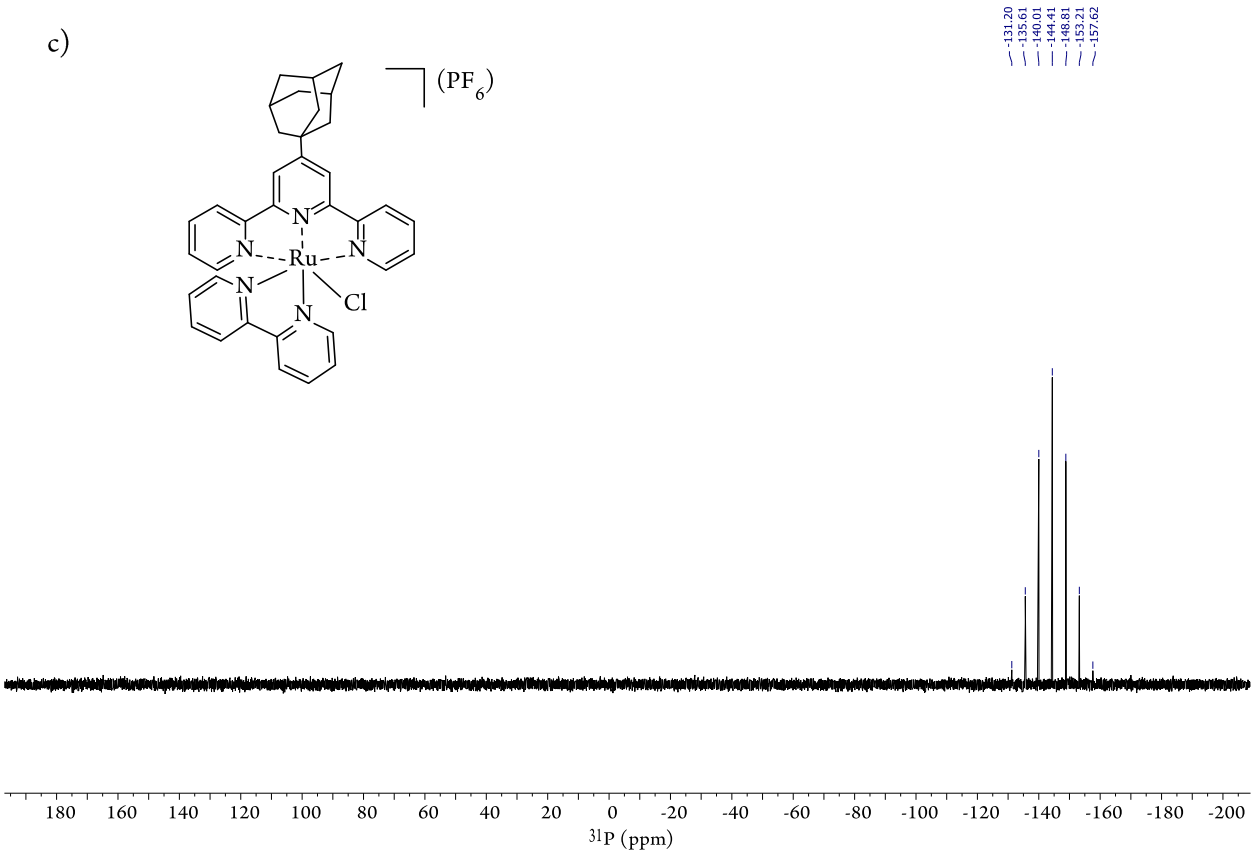

Figure S 8: a) ^{1}H and b) ^{13}C NMR and c) ^{31}P NMR of [Ru(bpy)(tpada)(Cl)](PF_6) **2** in $CDCl_3$.

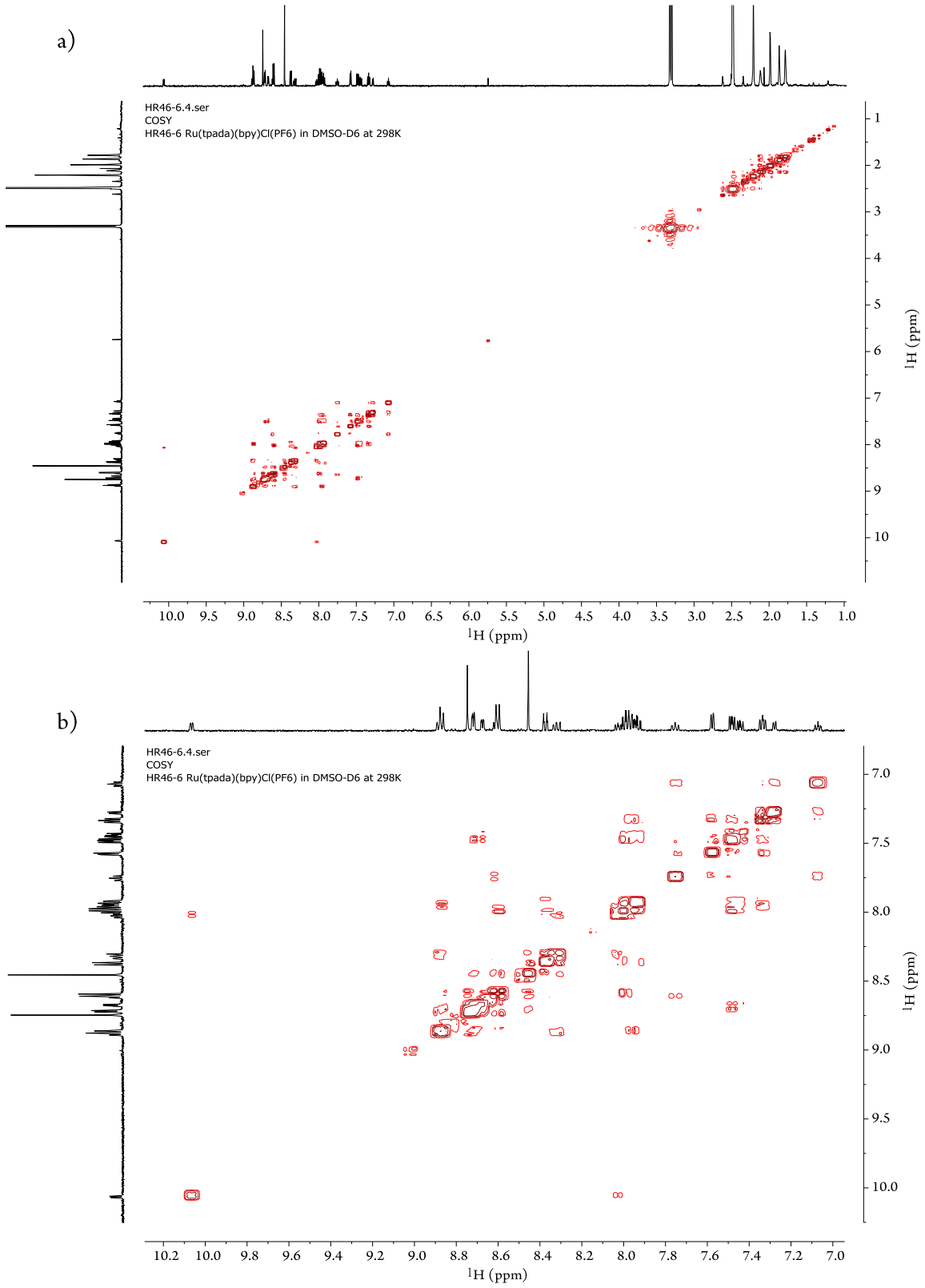

Figure S 9: COSY NMR (^{1}H-^{1}H) of [Ru(bpy)(tpada)(Cl)](PF_6) **2** in dmso-d_6 a) full spectrum b) zoomed in aromatic region.

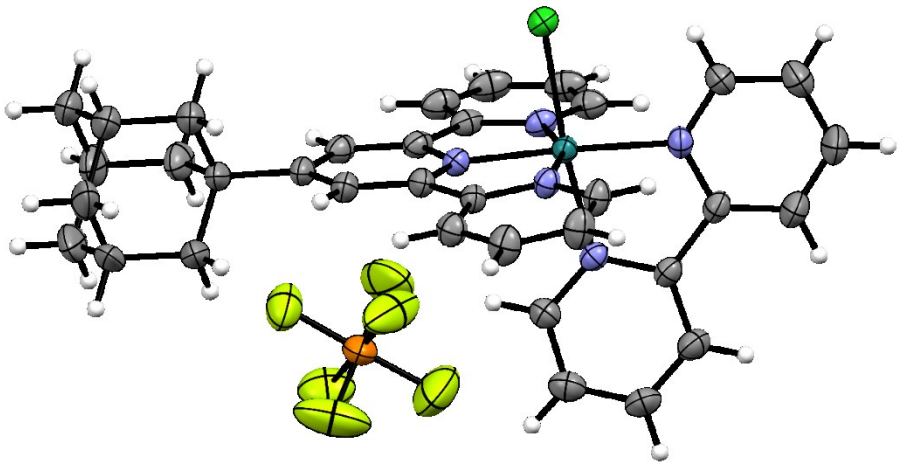

Figure S 10: Crystal structure of [Ru(bpy)(tpada)(Cl)](PF_6) **2.** Ellipsoidal representation of **2** ellipsoids are drawn at 50% probability. All co-solvate molecules have been omitted for clarity. Single crystals were obtained by vapor diffusion of pentane into a chloroform compound mixture.

Table S 3: Crystal Data and Structure Refinement for **2** [(Ru(bpy)(Cl)(tpada)](PF$_6$)

Empirical formula	$C_{37}H_{36.5}Cl_{5.5}F_6N_5PRu$
Formula weight	992.22
Crystal system	Orthorhombic
Space group	$P2_12_12_1$
a [Å]	8.48235(4)
b [Å]	17.59429(8)
c [Å]	26.99148(11)
α [°]	90
β[°]	90
γ [°]	90
Volume [Å^3]	4028.23(3)
Z	4
Density (calculated) [Mg/m^3]	1.636
Temperature [K]	160.00(10)
Wavelength [Å]	1.54184
Absorption coefficient [mm^{-1}]	7.438
F(000)	2000
Crystal size [mm^3]	0.69 x 0.049 x 0.016
Crystal description	red needle
Theta range for data collection [°]	2.998 to 79.363
Index ranges	-10<=h<=10, -22<=k<=22, -34<=l<=31
Reflections collected	114874
Independent reflections	8721 [R(int) = 0.0424]
Reflections observed	8638
Criterion for observation	I > 2 σ (I)
Completeness to theta	100.0 % to 67.684°
Absorption correction	Gaussian
Max. and min. transmission	1.000 and 0.100
Data / restraints / parameters	8721 / 13 / 514
Goodness-of-fit on F^2	1.034
Final R indices [I > 2 σ (I)]	R1 = 0.0322, wR2 = 0.0857
R indices (all data)	R1 = 0.0324, wR2 = 0.0859
Absolute structure parameter	-0.0142(19)
Largest diff. peak and hole [e.Å^{-3}]	0.556 and -0.673

Characterization of b: $[Ru(tpada)_2](PF_6)_2$

^{1}H NMR (400 MHz, acetone-d_6) δ 9.17 – 8.90 (s, d, J_{HH} = 8.0 Hz, 8H, 7;11;36;40;3;15;32;44), 8.04 (t, J_{HH} = 8.0 Hz, 4H, 1;17; 30; 46), 7.62 (d, J_{HH} = 4.0 Hz, 4H, 6;18; 35; 47), 7.29 (dd, J_{HH} = 4.0; 8.0Hz, 4H, 2;16;31;45), 2.42 – 2.20 (m, J_{HH} = 4.0 Hz, 19H, adamantane), 2.09 (s, 6H), 1.96 (s, 11H, adamantane).

^{13}C NMR (101 MHz, acetone-d_6) δ 161.94, 159.68, 156.20, 153.33, 138.86, 128.40, 125.42, 121.98, 43.10, 38.82, 37.06.

ESI-MS: *m/z* $[M\text{-}2PF_6]^{2+}$ $C_{50}H_{50}N_6Ru^{2+}$ calc. 418.1565 found 418.1565

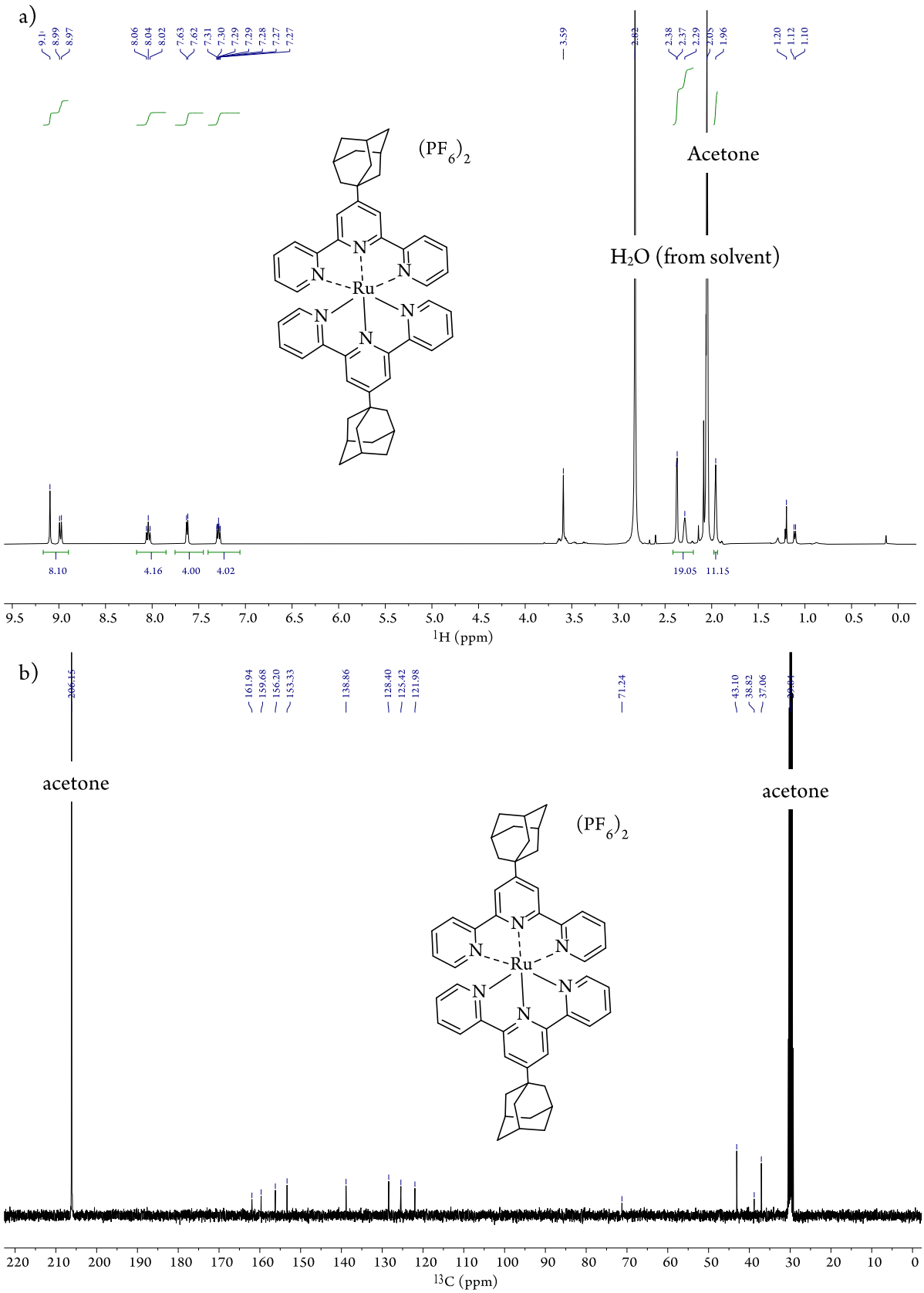

Figure S 11: a) ^{1}H and b) ^{13}C NMR of $[Ru(tpada)_2](PF_6)_2$ in acetone-d_6.

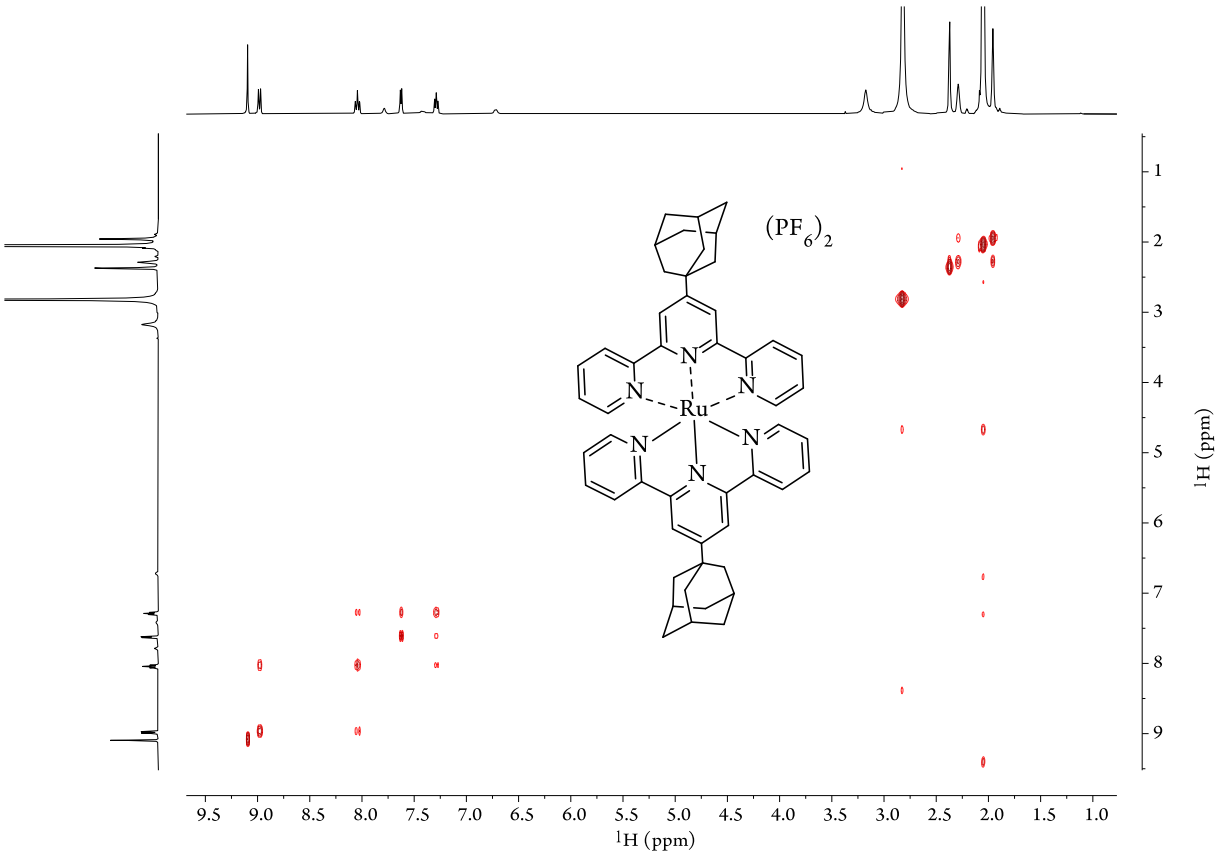

Figure S 12: COSY (^{1}H-^{1}H) NMR spectrum of $[Ru(tpada)_2](PF_6)_2$ in acetone-d_6.

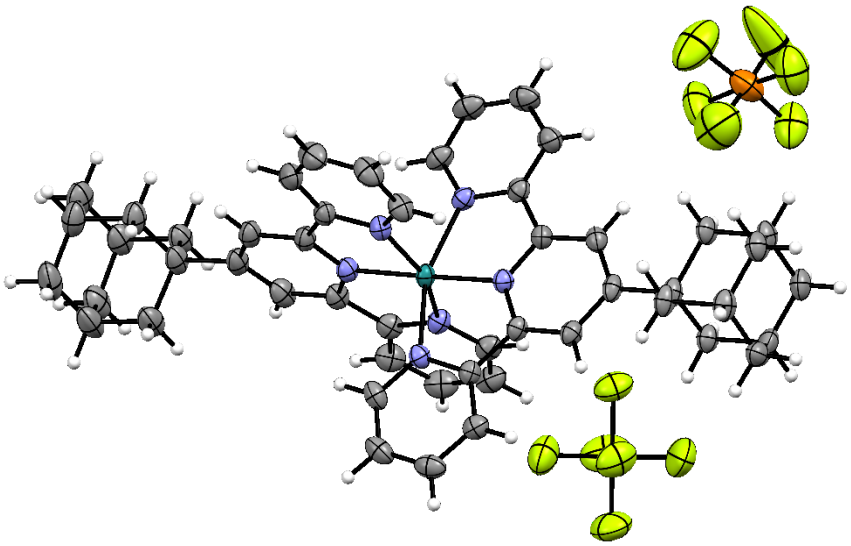

Figure S 13: Crystal structure of $[Ru(tpada)_2](PF_6)_2$. Ellipsoidal representation, Ellipsoids are drawn at 50% probability.

Single crystals were obtained by slow vapor diffusion of Et_2O into an acetone/MeOH mixture of the compound mixture.

Table S 4: Crystallographic Data and Structure Refinement for $[Ru(tpada)_2](PF_6)_2$

Empirical formula	$C_{50}H_{50}F_{12}N_6P_2Ru$
Formula weight	1125.97
Crystal system	Monoclinic
Space group	$P2_1/n$
a [Å]	12.74170(10)
b [Å]	17.3560(2)
c [Å]	21.6215(2)
α [°]	90
β [°]	98.2660(10)
γ[°]	90
Volume [$Å^3$]	4731.81(8)
Z	4
Density (calculated) [Mg/m^3]	1.581
Temperature [K]	160.00(10)
Wavelength [Å]	1.54184
Absorption coefficient [mm^{-1}]	4.125
F(000)	2296
Crystal size [mm^3]	0.063 x 0.052 x 0.008
Crystal description	red needle
Theta range for data collection [°]	3.805 to 76.191
Index ranges	-15<=h<=16, -21<=k<=21, -27<=l<=27
Reflections collected	73169
Independent reflections	9756 [R(int) = 0.0352]
Reflections observed	8519
Criterion for observation	$I > 2 \sigma (I)$
Completeness to theta	100.0 % to 67.684°
Absorption correction	Gaussian
Max. and min. transmission	1.000 and 0.826
Data / restraints / parameters	9756 / 6 / 755
Goodness-of-fit on F^2	1.027
Final R indices [$I > 2 \sigma (I)$]	R1 = 0.0487, wR2 = 0.1289
R indices (all data)	R1 = 0.0553, wR2 = 0.1336
Largest diff. peak and hole [$e.Å^{-3}$]	1.722 and -0.631

HG NMR titration studies

2.3 mg β-CD was dissolved in 2 mL (dmso-*d6*: D_2O) (7:3), and a ^1H NMR from 0.6 mL of the host mixture (0.001 M) was measured. The residual of 1.4 mL was taken to dissolve complex **1** or **2** in a concentration of 0.017 M. After acquiring the host spectrum, the solution is titrated with an increasing amount of the HG- mixture (between 1 µL and 135 µL) to the pure host solution, and a ^1H proton NMR is measured after every titration step. During the process, the host concentration is kept constant while the guest concentration increases. The chemical shift changes δ (ppm) of the host peaks are monitored and plotted against the H/G concentration to determine the binding constant via fitting with BindFit[10] (http://app.supramolecular.org/bindfit/). A 1:1 complexation model was determined with this method for both guests.

Titration of guest 1:

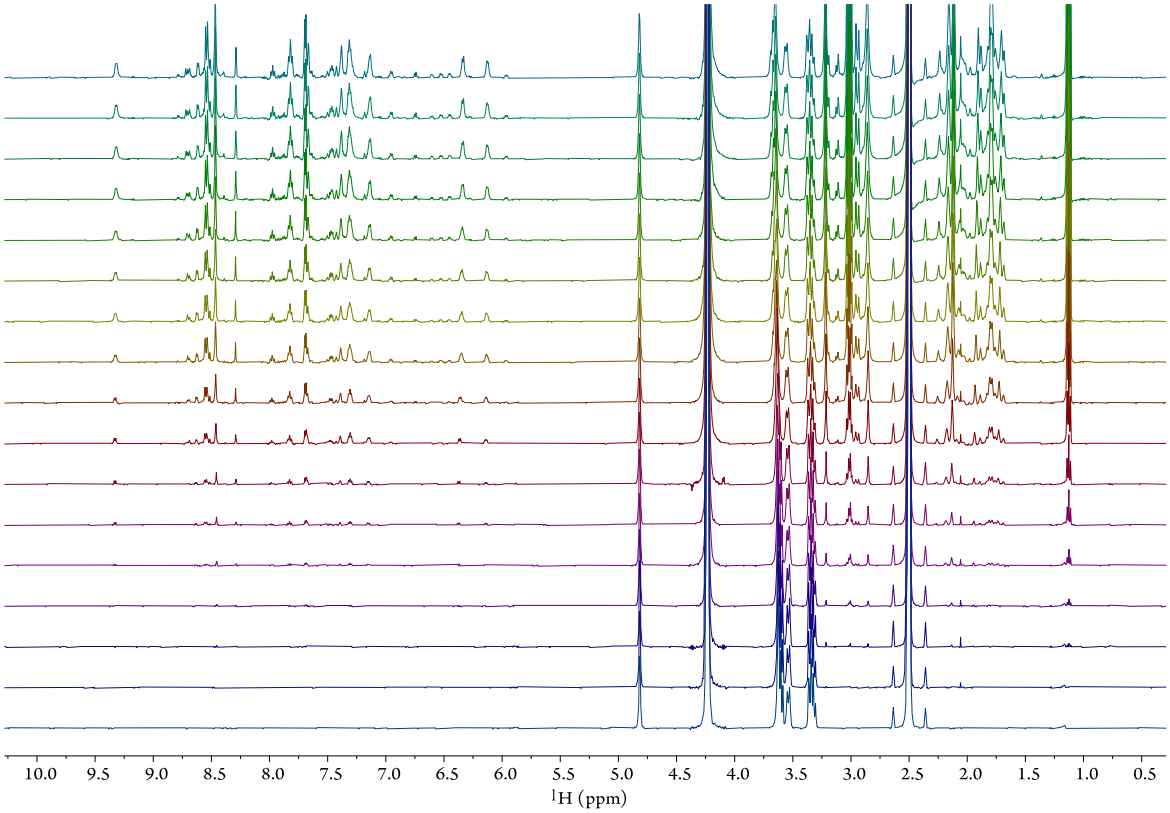

Figure S 14: ^1H NMR spectrum of the titration of 0.001 M β-CD with guest **1** in dmso-d_6: D_2O (7:3). Guest concentrations from the bottom to the top: 0; $2.77\cdot10^{-5}$; $6.91\cdot10^{-5}$; $1.37\cdot10^{-4}$; $2.03\cdot10^{-4}$; $2.66\cdot10^{-4}$; 3.90 10^{-4}; $5.04\cdot10^{-4}$; $6.07\cdot10^{-4}$; $8.09\cdot10^{-4}$; $9.79\cdot10^{-4}$; $1.12\cdot10^{-3}$; $1.31\cdot10^{-3}$; $1.45\cdot10^{-3}$; $1.55\cdot10^{-3}$;$1.61\cdot10^{-3}$; $1.70\cdot10^{-3}$ M. The guest region is between 9.5 and 6.0 ppm and the host region between 5.0 and 1.5 ppm.

Table S 5: Titration Data of Guest **1**

x1: H, c(mmol/ml)	x2: G, c(mmol/ml)	x3: G/H equivalent total	y1: Shift H1, (ppm)	y2: Shift H2, (ppm)	y3: Shift H3, (ppm)
0,0010	0	0,000	3,604	3,363	4,812
0,0010	2,77E-05	0,027	3,605	3,364	4,812
0,0010	6,91E-05	0,068	3,606	3,364	4,812
0,0010	1,37E-04	0,135	3,607	3,364	4,812
0,0010	2,03E-04	0,200	3,611	3,365	4,812
0,0010	2,66E-04	0,263	3,615	3,366	4,812
0,0010	3,90E-04	0,385	3,630	3,367	4,813
0,0010	5,04E-04	0,498	3,634	3,370	4,813
0,0010	6,07E-04	0,600	3,641	3,372	4,814
0,0010	8,09E-04	0,799	3,652	3,375	4,814
0,0010	9,79E-04	0,967	3,654	3,376	4,814
0,0010	1,12E-03	1,102	3,657	3,376	4,814
0,0010	1,31E-03	1,293	3,661	3,378	4,815
0,0010	1,45E-03	1,433	3,666	3,379	4,815
0,0010	1,55E-03	1,529	3,669	3,380	4,815
0,0010	1,61E-03	1,589	3,671	3,381	4,816
0,0010	1,70E-03	1,675	3,673	3,382	4,816

link to the fitting for guest **1**: http://app.supramolecular.org/bindfit/view/bb205417-ee2c-43b8-9994-8214dbad08b0

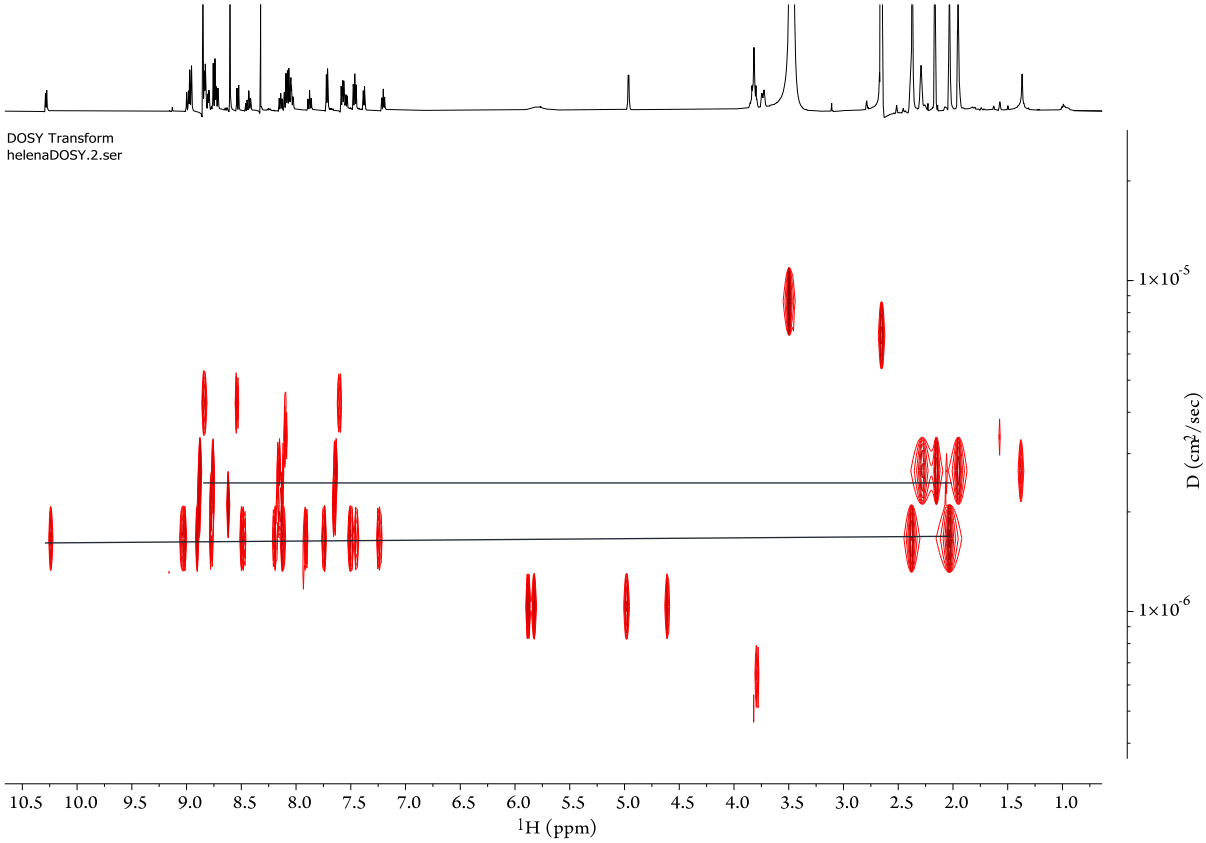

Figure S 15: DOSY NMR of guest **1** after titration with β-CD in dmso-d_6 : H_2O (7:3). Host concentration 0.001 M and guest concentration $1.70 \cdot 10^{-3}$ M. With this analysis, the diffusion coefficient D of the HG complex was determined to 1.45 10^{-6} cm^2 s^{-1}.

Titration of guest 2:

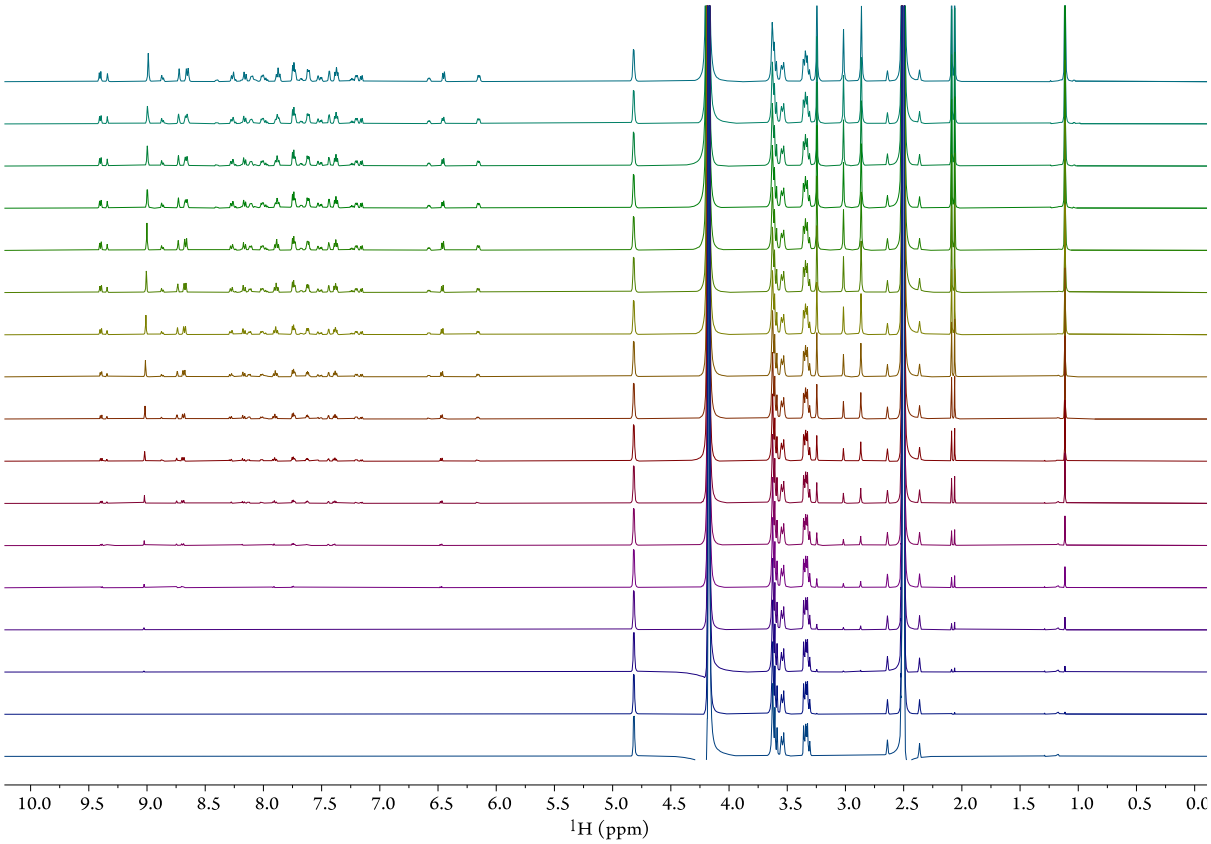

Figure S 16: ^{1}H NMR spectrum of the titration of 0.001 M β-CD with guest **2** in dmso-d_6: D_2O (7:3). Guest concentrations from the bottom to the top: 0; $2.77\cdot10^{-5}$; $6.91\cdot10^{-5}$; $1.37\cdot10^{-4}$; $2.03\cdot10^{-4}$; $2.66\cdot10^{-4}$; 3.90 10^{-4}; $5.04\cdot10^{-4}$; $6.07\cdot10^{-4}$; $8.09\cdot10^{-4}$; $9.79\cdot10^{-4}$; $1.12\cdot10^{-3}$; $1.31\cdot10^{-3}$; $1.45\cdot10^{-3}$; $1.55\cdot10^{-3}$;$1.61\cdot10^{-3}$; $1.70\cdot10^{-3}$ M. The guest region is between 9.5 and 6.0 ppm and the host region is between 5.0 and 1.5 ppm.

Table S 6: Titration Data of Guest **2**

x1: H, c(mmol/ml)	x2: G, c(mmol/ml)	x3: G/H equivalent total	y1: Shift H1 (ppm)	y2: Shift H2 (ppm)	y3: Shift H3 (ppm)
0,0010	0	0,000	3,360	4,814	3,624
0,0010	2,77E-05	0,027	3,360	4,814	3,624
0,0010	6,91E-05	0,068	3,360	4,814	3,625
0,0010	1,37E-04	0,135	3,360	4,814	3,625
0,0010	2,03E-04	0,200	3,360	4,814	3,625
0,0010	2,66E-04	0,263	3,360	4,814	3,625
0,0010	3,90E-04	0,385	3,360	4,814	3,626
0,0010	5,04E-04	0,498	3,360	4,814	3,626
0,0010	6,07E-04	0,600	3,361	4,815	3,626
0,0010	8,09E-04	0,799	3,361	4,815	3,626
0,0010	9,79E-04	0,967	3,361	4,815	3,627
0,0010	1,12E-03	1,102	3,362	4,815	3,627
0,0010	1,31E-03	1,293	3,362	4,815	3,628
0,0010	1,45E-03	1,433	3,362	4,815	3,628
0,0010	1,55E-03	1,529	3,362	4,816	3,628
0,0010	1,61E-03	1,589	3,363	4,816	3,629
0,0010	1,70E-03	1,675	3,363	4,816	3,629

Link to the fitting for guest **2**: http://app.supramolecular.org/bindfit/view/f09386e0-1bea-4997-9f2c-55ccc4cd6195

Theoretical calculations

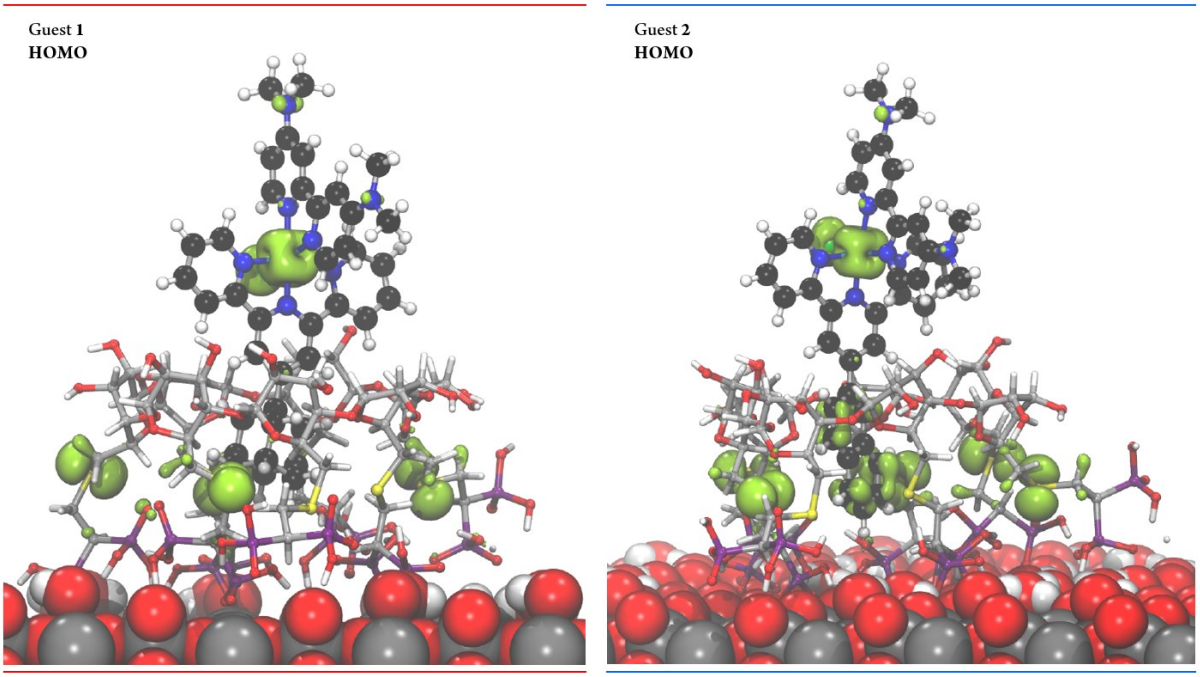

Figure S 17: DFT optimization of guests 1 and 2 interacting with the toTiO_2 (110) surface-bound host. Most of the water molecules have been removed from the illustration for clarity, thus leaving only the ones adsorbed at the surface. The green solid surfaces correspond to the electron density distribution around the HOMO.

Electrochemistry

All measurements in organic solvents were conducted in extra dry solvents. The supporting electrolytes were purchased from Sigma Aldrich. Homogenous measurements were conducted with a concentration of 0.1 mM of the complexes in the related solvents and 0.1 M or 0.2 M supporting electrolyte. In the following, CV of the complexes is depicted.

Experimental

All reagents were prepared in the glove box when measured in organic solvents. For the ammonia oxidation in THF, solution **1** consisting of 0.1 M $TBAPF_6$ in THF and solution **2** consisting of 0.1 M $TBAPF_6$ and 0.1 M NH_4PF_6 in 0.5 M NH_3 in THF or solution **3** (200 mM NH_3) was prepared. The 0.5 M NH_3 THF solution was purchased from Sigma Aldrich. For the AO in H_2O, different solvent mixtures were prepared in air and measured under standard lab conditions (20 ºC). The pH of the resulting aqueous solutions was measured with a pH meter. The reference electrode consists of an AgCl wire in 0.1 M $TBAPF_6$ THF solution or 0.2 M $NaClO_4$ H_2O.

Table S 7: Solvent Mixtures For Electrochemical Measurements

AO in THF	**$TBAPF_6$**	**NH_4PF_6**	**solvent**
1	0.1M	--	THF
2	0.1M	0.1M	0.5 M NH_3 in THF
3	0.1M	0.1M	0.2 M NH_3 in THF
AO in H_2O	**$NaClO_4$**	**NH_4PF_6**	**solvent**
4	0.2M	--	H_2O pH=6.0 (22ºC)
5	0.2M	--	0.5 M NH_3 in H_2O pH=11.3 (22ºC)
6	--	--	0.5 M NH_3 in H_2O pH=11.4 (22ºC)
7	0.2M	0.1M	0.5 M NH_3 in H_2O pH=10.3 (22ºC)
8	--	0.1M	0.5 M NH_3 in H_2O pH=10.4 (22ºC)
9	--	--	0.1 M phosphate buffer (pH=8.0)
10	--	--	0.2 M NH_3 phosphate buffer (pH=10.86)

ITO Spin-Coating Suspension

ITO nanoparticles (10nm, 99.99%) were sonicated in 10mL EtOH for 10 min when a mixture of ethyl cellulose (200 mg), alcohol surfactant (proprietary nanopowder dispersant, 225 mg), and terpineol (5.0 g) in 5mL EtOH was added and the suspension was sonicated for 5 min. The volatiles were removed by rotary evaporation to form a blue paste. The paste was diluted with EtOH (1:4) and is used for spin-coating as reported in our previous work.[11]

Electrode preparation: The electrode surfaces were prepared by cutting 1.25 cm x 2.5 cm or 1.0 cm x 3.5 cm FTO (fluorine-doped tin oxide) glass plates and washing them for 10 min in acetone, 10 min in soap and H_2O, 10 min in H_2O, followed by 10 min of EtOH (7:3) in an ultrasonic bath. Afterwards, the plates were dried under an N_2 stream (30 sec.), and half of the plate (~1 cm) was wrapped in Kapton-tape, followed by spin coating with an mITO (mesoporous indium tin oxide) mixture (in EtOH). For the first mITO layer, 25-30 µL of the mixture was pipetted onto the plates, and the samples were spin-

coated and afterwards dried on a heat plate at 120ºC for 10 min. This process was repeated twice with the second and third layers using 25 µL of mITO mixture volume. For the H-cell 3.5 cm x 1cm plates were prepared. Therefore, 180 µL of the spin-coating suspension was used. In the last cycle, the mITO (on FTO) plates were dried for 60 minutes at 450 ºC after the tape was removed.

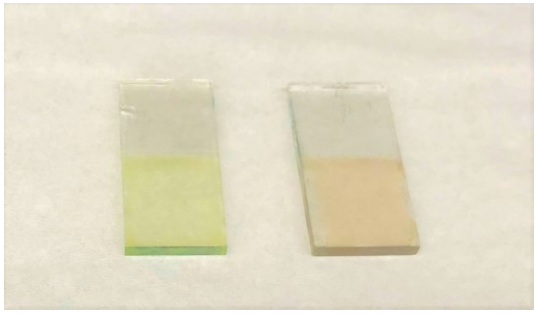

Figure S 18: Working electrode with immobilized host (left) and immobilized host and absorbed guest (right)

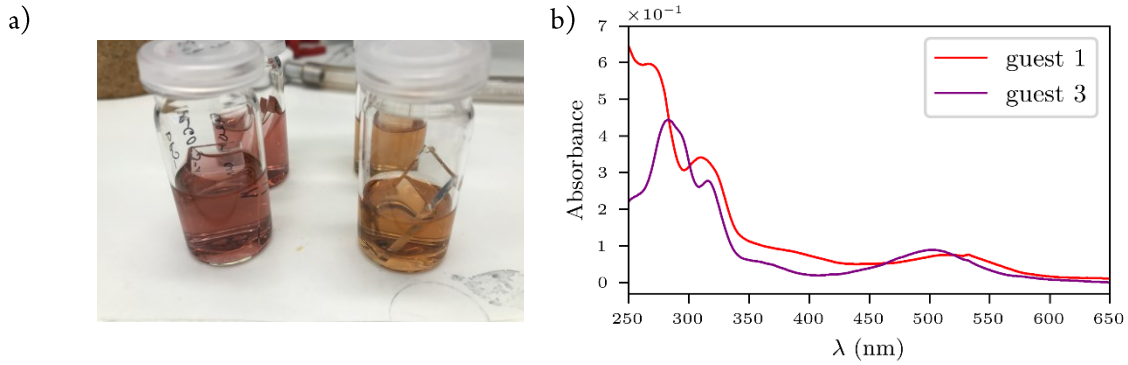

Figure S 19: a) Electrode functionalization with guests **1** and **3** and b) UV/Vis spectrum of guests **1** (red) and **3** (violett) in THF.

CV of Guest 1 and Guest 3

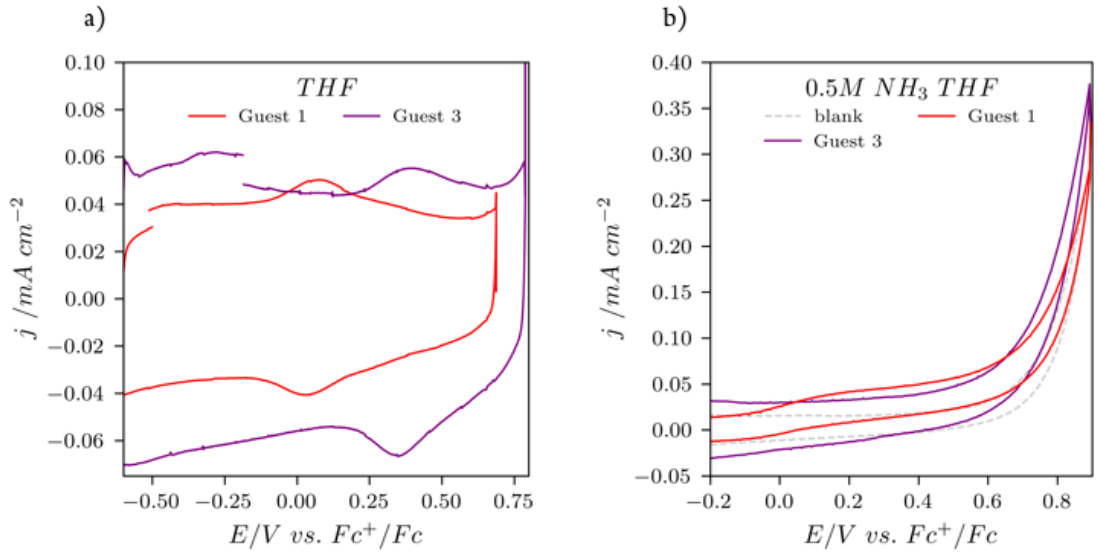

Figure S 20: Electrochemistry of guest **1** (red) and guest **3** (purple) a) CV (100 mVs^{-1}) in 0.1M $TBAPF_6$ in THF and b) CV (20 mVs^{-1}) in 0.1 M $TBAPF_6$ and 0.1 M NH_4PF_6 in 0.5 M NH_3 in THF. WE: mITO+H+G, CE: Pt wire, RE: AgCl wire in 0.1 M $TBAPF_6$ in THF.

Preparation of the mixtures

Host solution (0.1 mM): 5.3 mg K_2PO_3-β-CD were dissolved in 10 mL H_2O (adjusted to pH 2.4 with H_2SO_4 diluted, measured with pH meter).

Guest solution: 0.1 mM of the guest was dissolved in 10 mL MeOH

Host binding: The spin-coated mITO plates were dipped in the host mixture for 1h, followed by dipping in H_2O for 10 min, DMSO for 10 min, and MeOH for 5 min and dried under an N_2 stream for 30 seconds.

Guest absorption: The host modified mITO was dipped for 1h in the guest solution, followed by 5 min in MeOH, and dried under an N_2 stream for 30 seconds.

Physisorbed guest: The mITO plate is dipped directly in the guest mixture for 1h without any previous host dipping and washed for 5 min with MeOH, and dried under an N_2 stream for 30 seconds afterwards.

Washing with DMSO: The plate with the host and guest was dipped into DMSO for 40 min, quickly in MeOH, and dried under an N_2 stream for 30 seconds.

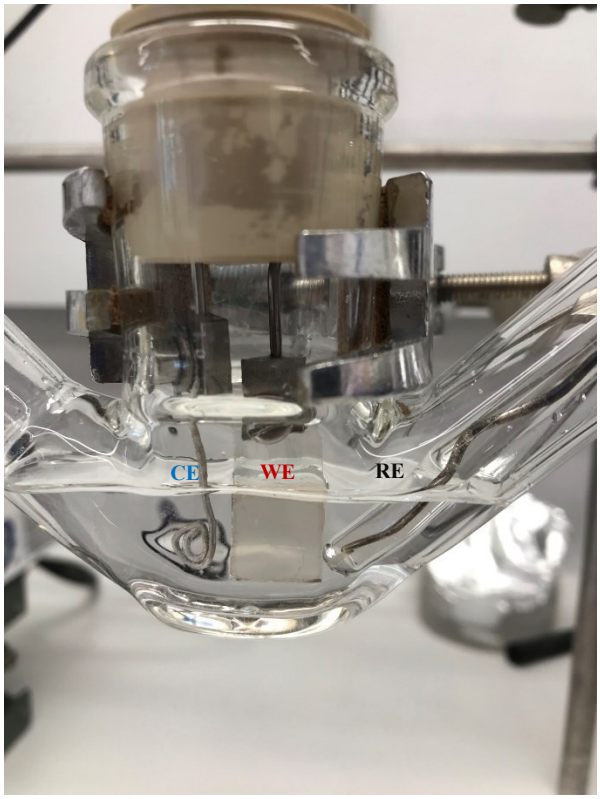

Figure S 21: Experimental set-up for electrochemical measurements in organic solvents. WE: mITO + host + guest, CE: Pt wire, RE: AgCl in 0.2 M $NaClO_4$ in H_2O or 0.1 M $TBAPF_6$ in THF.

A change in the reference electrodes' potential in organic and aqueous solutions was recognized when measuring in an ammonia solution for several hours. We assume that this is caused by ammonia entering the reference electrode over time and the resulting pH change.

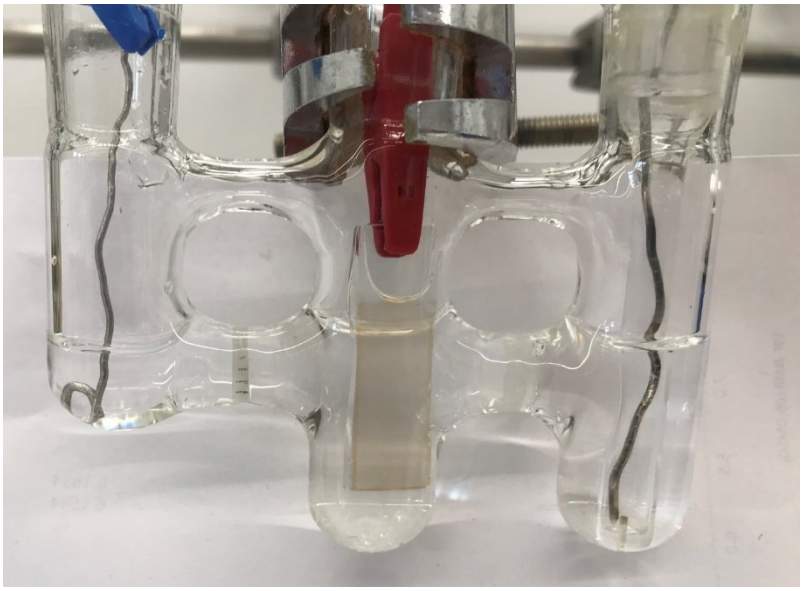

Figure S 22: Electrochemical set-up: H-cell for nitrate and nitrite determination. WE: mITO + host + guest, CE: Pt wire, RE: AgCl in 0.2 M $NaClO_4$ in H_2O.

Procedure for stability measurements: Chronoamperometry

The blank is measured with the mITO plate and functionalized host. A CV is measured in THF (0.1M $TBAPF_6$) or 0.2 M $NaClO_4$ in H_2O for aqueous experiments. Afterwards, the same sample is measured in the related ammonia containing mixture, *e.g.* 0.1 M NH_4PF_6 and 0.1 M $TBAPF_6$ in 0.5 M NH_3 in THF. After the CV in the ammonia solution, CA at a potential certain potential is measured for a certain time, and afterwards, a CV in both media (with ammonia and without) is measured again to compare the redox peak and catalysts loading before and after CA. For reabsorption, the sample is washed with acetone, dried (N_2 stream), and dipped in the guest solution again for 1h. The complete process is repeated several times.

Guest absorption with [Ru(bpy-NMe_2)(Cl)(tpada)](PF_6): The host functionalized electrode was soaked in 0.1 mM guest in MeOH for a defined time period (usually 1h) and washed for 5 min in MeOH and measured with UV/Vis. The baseline was set to the mITO + host sample (**Figure S 23**a). After 90 minutes, the highest guest absorption was achieved and no longer changed after a longer soaking time. Since the difference between 60 and 90 min was lower than 10%, we decided to shorten the protocol and use 1h for the guest absorption in most of the experiments. For GC measurements and nitrate tests, we used longer absorption times.

The reabsorption ability of the guest to the surface-bound host was tested when washing the samples in between for 40 min with DMSO, followed by 5 min in MeOH. The related absorption of the MLCT between 420 and 560 nm (**Figure S23b**) of guest **1** was measured before every CV and after CA and the reabsorbing and washing steps. Recovery of the HG complex on the surface was achieved up to 3 times before a dropping of the absorption peak in the fourth reabsorption cycle (**Figure S23b**, RG 4, black) was notable. The first and second reabsorption after CV and washing with DMSO are higher (RG1 violet, RG2 green) than the first guest absorption (red, G), which indicates that after DMSO washing, the cavity is empty and can absorb more guest.

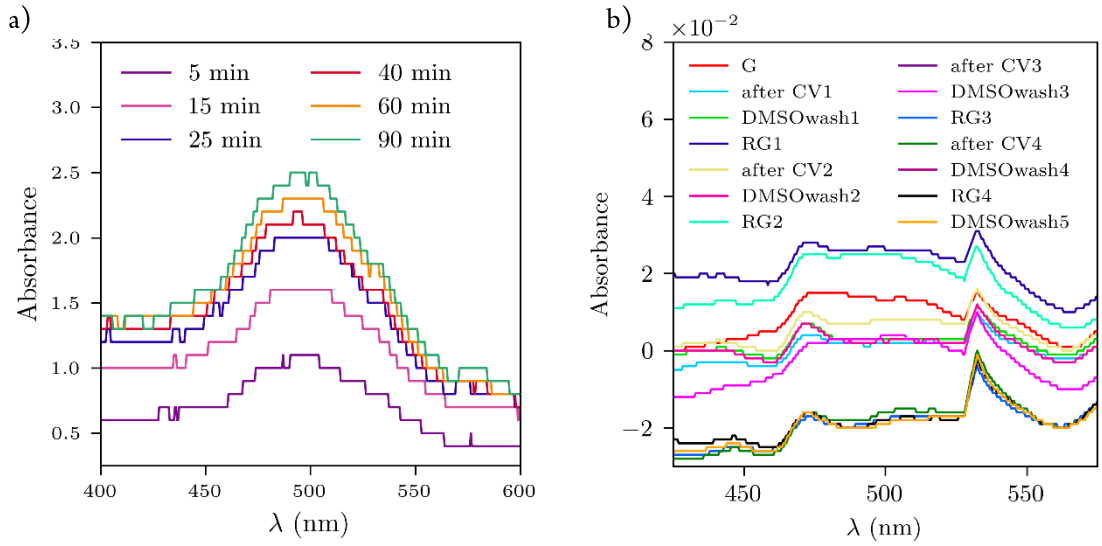

Figure S 23: UV/Vis absorbance spectra of: a) Guest **3** absorption studies after a certain time of soaking the mITO-host electrode in the guest **3** MeOH solution. b) Guest absorption after CV, CA and reabsorption of guets **1**. RG= reabsorption guest

Electrode surface determination

Cyclic voltammetry of FTO and FTO with spin-coated (3 layers) mITO electrode plate was measured at different scan rates (500, 200, 100, 90, 80, 70, 60, 50, 20, 10 mVs^{-1}) in 0.2 M $NaClO_4$ in H_2O solution (AgCl wire as reference electrode). With the resulting calibration curves a factor 157 per cm^2 was determined between the FTO and the mITO on FTO layer. This corresponds to a surface area of 392 cm^2 for a geometric area of 2.5 cm^2 and 235 cm^2 for a geometric area of 1.5 cm^2. For the graphical illustration, the geometric area is shown, for the determination of the catalyst loading per cm^2 the calculated surface area was used.

Wave analysis for catalyst loading determination

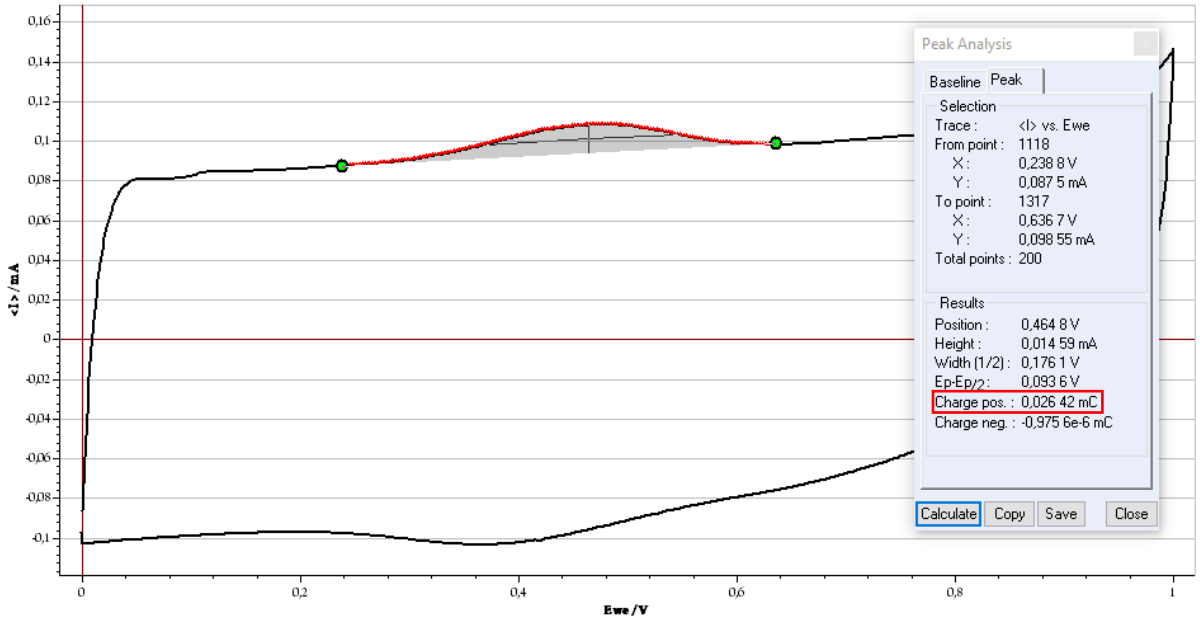

Figure S 24: Example of an integration of a CV $Ru^{II/III}$ redox peak captured in 0.1 M NH_4PF_6 and 0.1 M $TBAPF_6$ in THF with a scan rate of 100 mVs^{-1} of guest **1**.

The catalyst loading was calculated via the Peak Analysis module in EC lab. The charge is determined by the integration of the $Ru^{II/III}$ redox peak and given in mC.

In the case of an overlapping RuII/III and Ru III/IV redox peak, only half of the integration was used for further calculations.

In this example, a surface loading of 0.026 mC with a surface area of 1.25 cm^2 and a scan speed of 100mV, corresponds to a catalyst loading of 1.15 pmol cm^{-2}:

$$\frac{\text{charge (C)}}{\text{F}\left(\frac{\text{C}}{\text{mol}}\right)} = \frac{0{,}000026\ \text{C}}{96485.33\frac{\text{C}}{\text{mol}}} = 2.70 \cdot 10^{-10}\ \text{mol electrons} \qquad \textbf{(eq. 1)}$$

$$\frac{2.70 \cdot 10^{-10}\ (\text{mol})}{235\ (\text{cm}^2)} = 1.15 \times 10^{-12}\ \text{mol/cm}^2 = 1.15\ \text{pmol/cm}^2 \qquad \textbf{(eq. 2)}$$

Electrochemical measurements

Electrocatalysis of the physisorbed guest 1 in THF

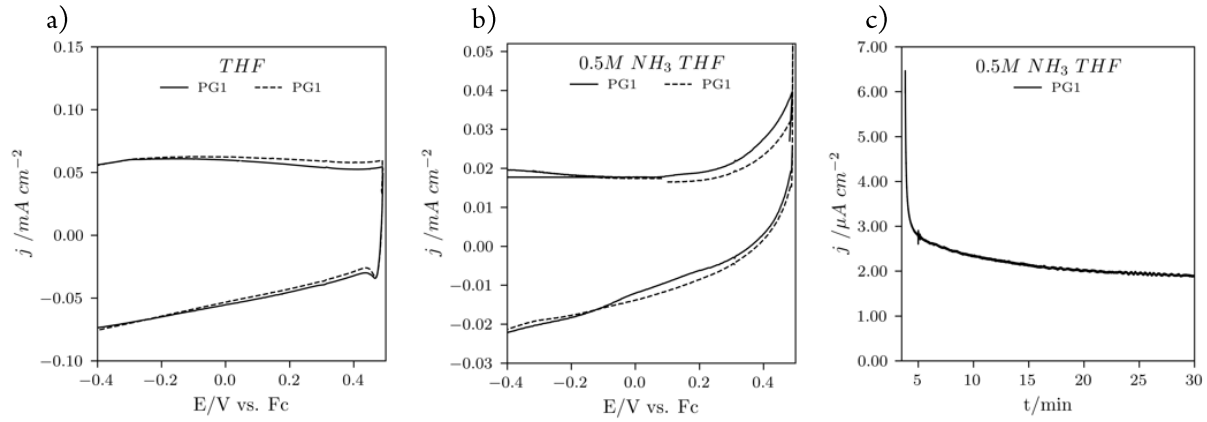

Figure S 25: Electrochemistry of the physisorbed guest 1 (PG1, black) (right) a) CV (100 mVs^{-1}) in 0.1 M $TBAPF_6$ in THF before (solid line) and after CA (dashed line) and b) CV (20 mVs^{-1}) in 0.1 M $TBAPF_6$ and 0.1 M NH_4PF_6 in 0.5 M NH_3 in THF (pH= 7.2). c) CA for 60 min at 0.1 V (vs Fc). Conditions: WE: mITO+H+G (left), mITO+G (right), CE: Pt wire, RE: AgCl wire in 0.1 M $TBAPF_6$ in THF.

Electrocatalysis of the physisorbed guests in water

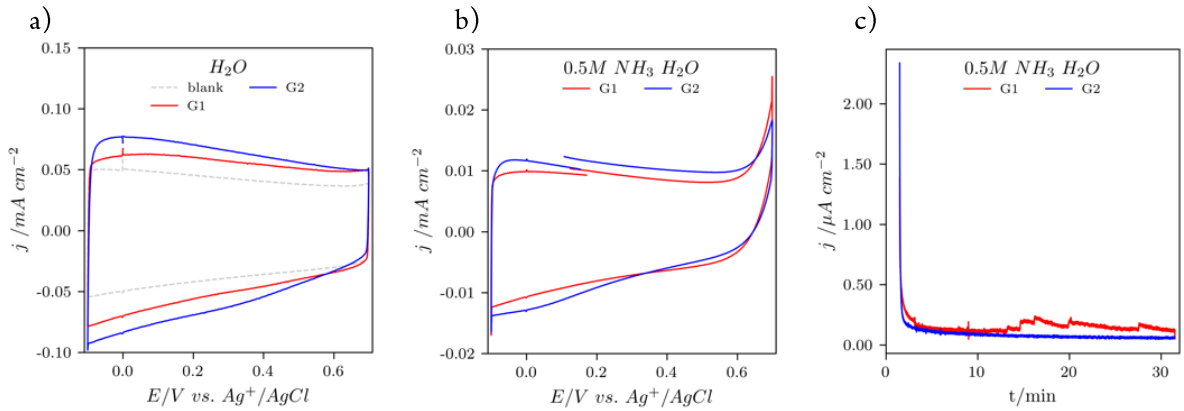

Figure S 26: Electrochemistry of physisorbed guest 1 (G1, red) and guest 2 (G2, blue) a) CV (100 mVs^{-1}) in 0.2 M $NaClO_4$ in H_2O, b= blank (dashed grey line, WE: mITO+H) and b) CV (20 mVs^{-1}) 0.2M $NaClO_4$ 0.5 M NH_3 in H_2O (pH= 11.3, 22 ºC). c) CA for 30 min at 0.2 V (vs Ag/AgCl). Conditions: WE: mITO+G, CE: Pt wire, RE: AgCl wire in 0.2 M $NaClO_4$ in H_2O.

Physisorbed guest means that no previous host functionalization of the electrode was performed to demonstrate that the host is necessary to bind the guest to the surface.

GCMS with labeled ^{15}N NH_3 (0.5M) in H_2O

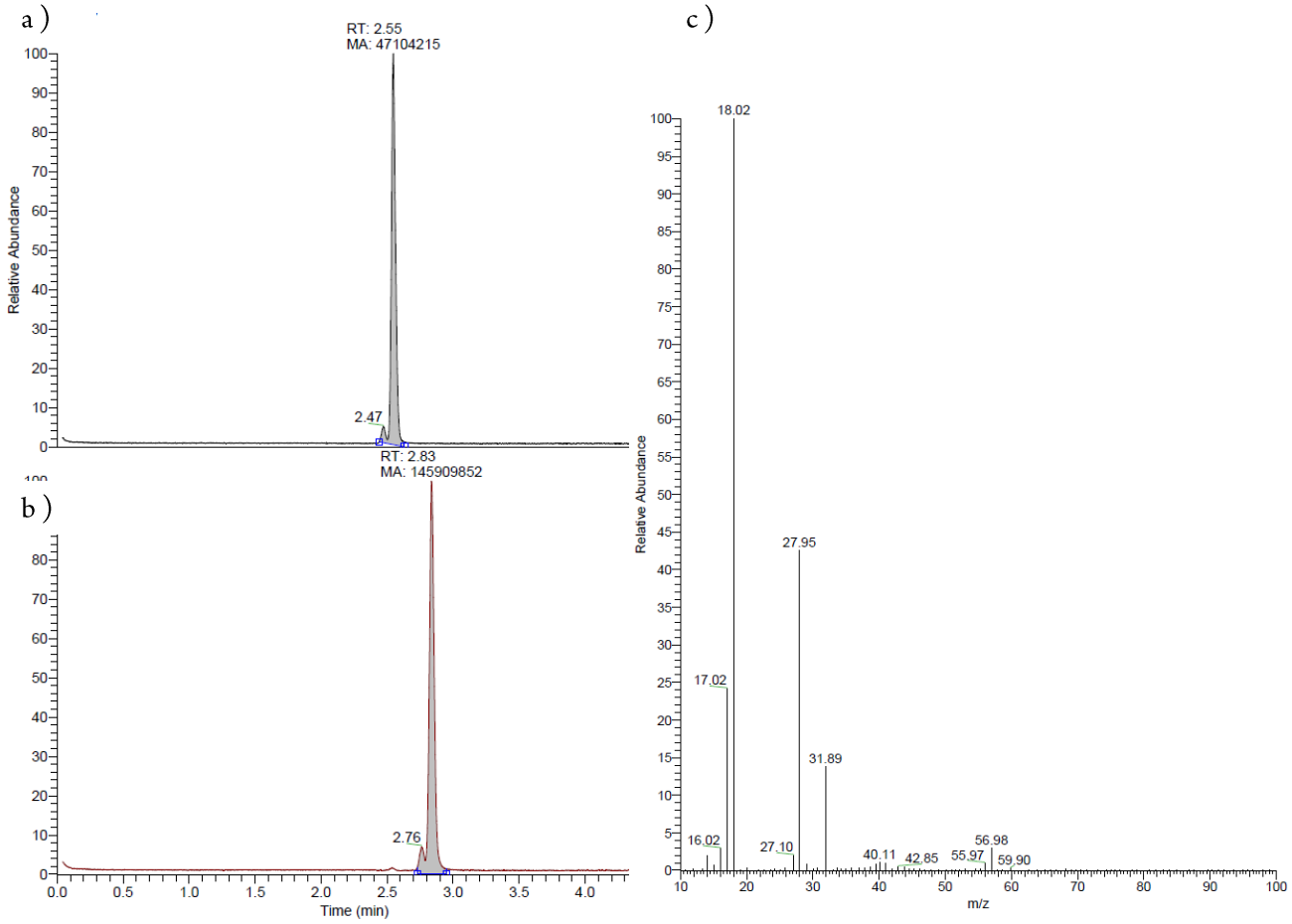

Figure S 27: Headspace analysis of guest **1** before and after 60 min CA at 0.2 V vs AgCl in labeled 0.5M $^{15}NH_3$ in H_2O. a) GC peak before CA b) GC peak after CA c) MS spectrum after CA shows the absence of $^{30}N_2$. The nitrogen is coming from the air, no m/z= 30 was observable. The slightly different retention times before and after catalysis are due to the manual insertion.

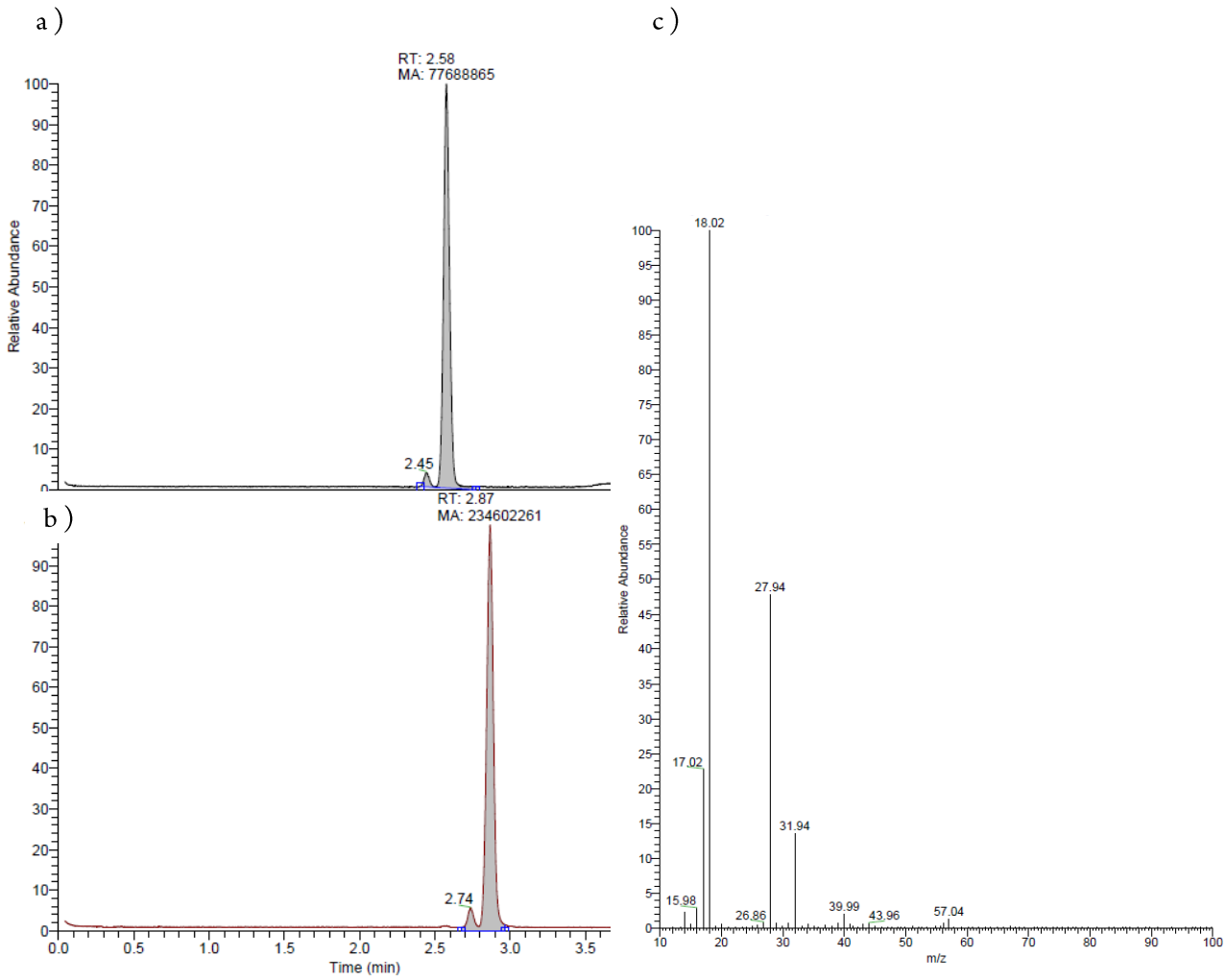

Figure S 28: Headspace analysis of guest **2** before and after 60 min CA at 0.2 V vs AgCl in labeled 0.5M $^{15}NH_3$ in H_2O. a) GC peak before CA b) GC peak after CA c) MS spectrum after CA shows the absence of $^{30}N_2$. The nitrogen is coming from the air, no m/z= 30 was observable. The slightly different retention times before and after catalysis are due to the manual insertion.

Determination of nitrate in aqueous solution

Solution A was prepared by dissolving 34.4 mg (0.2 mmol) of sulfanilamide in 10 mL of 37% HCl, and afterwards diluting to 200 mL with water.
Solution B was prepared by dissolving 51.8 mg (0.2mmol) of *N*-(1-naphthyl)-ethylenediamine dihydrochloride in 10mL of 37% HCl, followed by dilution to 200 mL with milli-Q water. Reagents A and B were stored at RT in the dark and were stable up to 6 weeks.
Solution C was prepared by dissolving 172 mg (1 mmol) of sulfanilamide and 130 mg (0.5 mmol) of *N*-(1-naphthyl)ethylenediamine dihydrochloride in 10 mL of 37% HCl and afterwards diluting to 200 mL with water. Additionally, 470 mg (3 mmol) of VCl3 was added to the mixture solution (stored in the fridge). [12] When kept in the fridge the solution was stable for 2 months.

Standard solutions:
Nitrite standard solutions:138.0 mg (2 mmol) of $NaNO_2$ in 200.0 mL H_2O. A certain amount (0.01, 0.02, 0.03, 0.04 and 0.05 mL) was taken from this 10mM solution and diluted to 20mL to give solutions of 5, 10, 15, 20 and 25 µM.[12]
For the UV/Vis measurement, 5 mL of each concentration point was taken and 0.5 mL of solution A followed by 0.5 mL of solution B was added, mixed through shaking and let stand for 10 min before measured with UV/VIS. This further dilution with the color solutions A and B led to a final concentration of 0.004, 0.008, 0.013, 0.017, and 0.021 mmol/L of the $NaNO_2$ standard.

Nitrate standard solutions: 202.2 mg (2 mmol) of KNO_3 were dissolved in 200.0 mL H_2O and a certain amount (0.01, 0.02, 0.03, 0.04, and 0.05 mL) was taken from this 10 mM solution and diluted to 20 mL to give solutions of 5, 10, 15, 20 and 25 µM.[12]
Afterwards 1.5 mL of solution C was added to 1.5 mL of each standard solution. This further dilution with the color solutions C led to a final concentration of 0.0025, 0.005, 0.0075, 0.01and 0.0125 mmol/L of the KNO_3 standard. The samples were heated in a 65°C water bath for 15 min, afterwards let cool to RT and measured with UV/VIS.

Sample measurement:
NO_2^-: After CA at 0.5V for 90 min in 6 mL of 200 mM NH_3 (in phosphate buffer pH= 10.8) solution, 2 mL of the anode solution were taken, and 0.4 mL A and 0.4 mL B were added, shaken, and let stand for 15 min at RT. Afterwards the mixture was measured with UV/VIS. The same procedure was repeated with the 200 mM NH_3 solution before electrocatalysis as a reference and to demonstrate that no nitrite is present in the solution before CA. The measured Absorbance of the sample was inserted in the calibration curve to determine the formed amount of NO_2^-.
NO_3^-: To remove all present NO_2^- from the solution, which would influence the nitrate determination, Zn dust reduction was performed by taking 2 mL of the anode solution after CA and adding 20 µL HCl (37%) and 100 mg Zn powder. The mixture was shaken for 2 min and afterwards filtered with a syringe filter (PES-membrane filter, 0.22 µm). To the 2 mL of anode solution which now only contain the formed NO_3^-, 2 mL of solution C was added and heated in a water bath (65°C) for 15 min. After cooling back to room temperature, the sample was let stand for 2 h at RT and measured with UV/VIS.

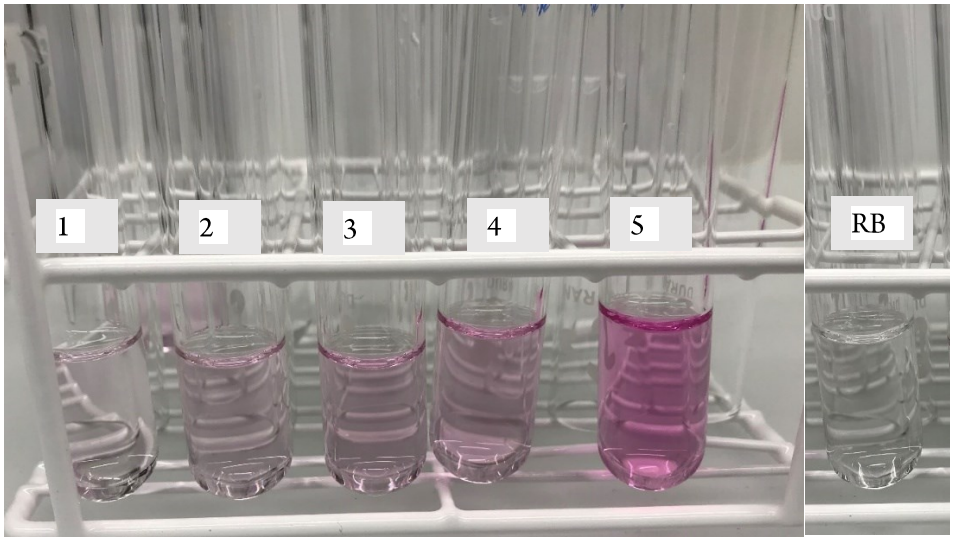

Figure S 29: Sample, reference, and standard $NaNO_2$ after adding solutions A and B.

1: 0.005 mM $NaNO_2$ + A+B

2: 0.010 mM $NaNO_2$ + A+B

3: 0.015mM $NaNO_2$ + A+B

4: 0.020 mM $NaNO_2$ + A+B

5: 0.025 mM $NaNO_2$ + A+B

RB: Reference Anode Solution 50 mM NH_3 before CA + A+B

*The NO_2^- concentration was below the detection limit or did not form during the catalysis.

NO_2^- detection:

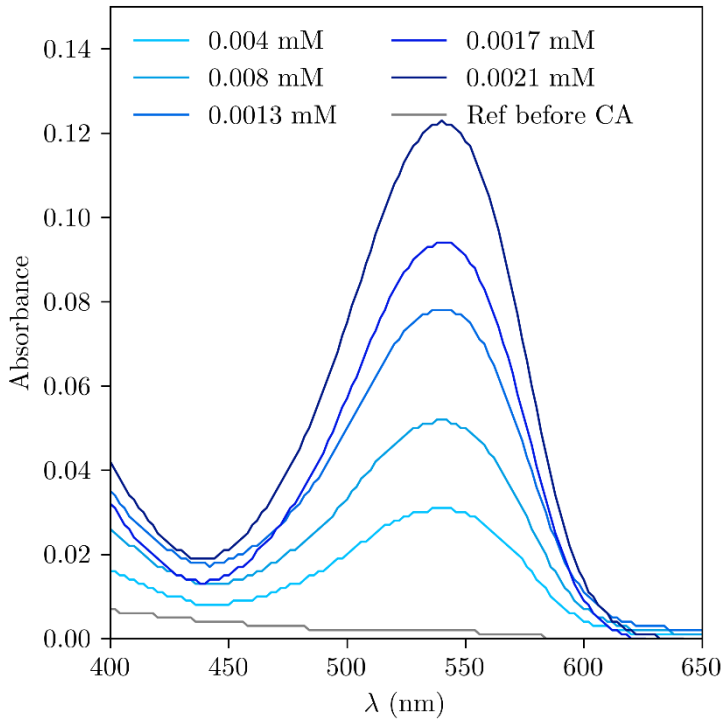

Figure S 30: UV/VIS spectrum of the anode solution after CA and the $NaNO_2$ standard solutions after adding 0.5 mL A and 0.5 mL B.

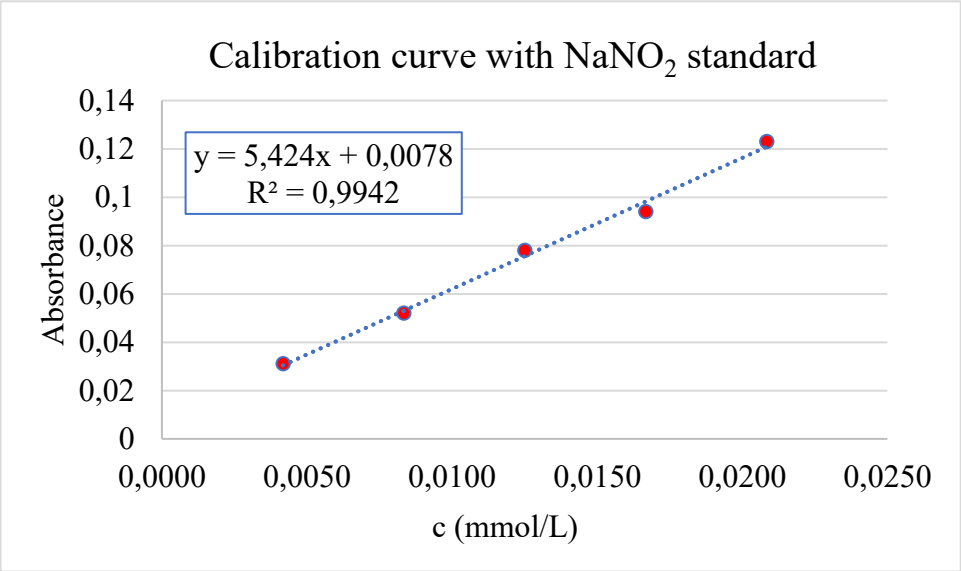

Figure S 31: Calibration curve of the nitrite standard (mmol/L) after adding 0.5 mL A and 0.5 mL B.

NO_3^- detection:

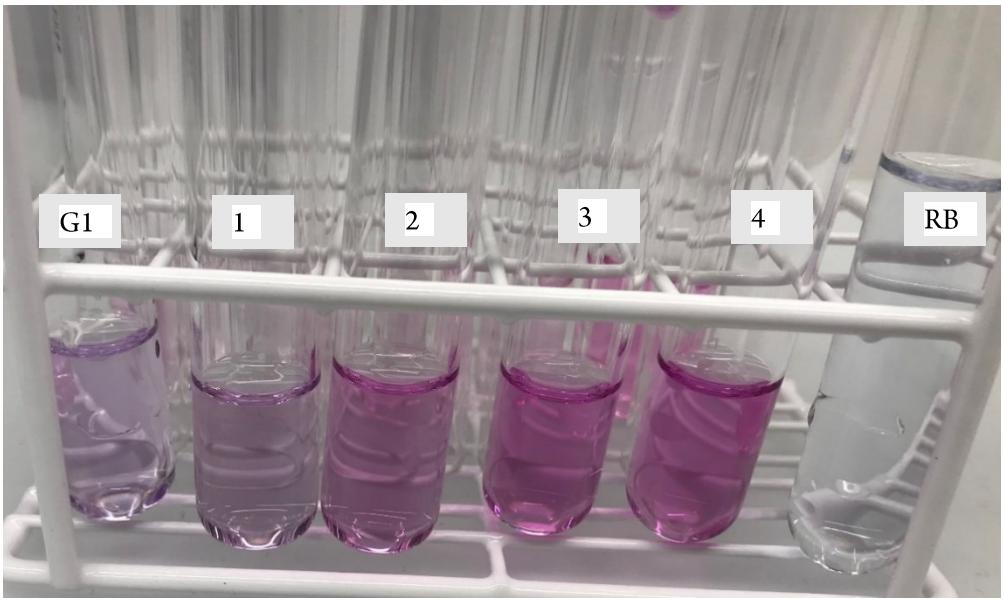

Figure S 32: Sample, standard solutions of KNO_3 and Reference after adding 1.5 mL solution C.

G1: G1 sample CA (90 min at 0.5V) + Zn^0 afterwards +C (65ºC)

RB: Reference Anode Solution 50 mM NH_3 before CA + C

1: 0.005 mM KNO_3 + C

2: 0.010 mM KNO_3 + C

3: 0.015 mM KNO_3 + C

4: 0.020 mM KNO_3 + C

Blank measurements:

A blank sample FTO + mITO was tested twice with the same tests after CA for 90 min at 0.5V vs Ag/AgCl in 200 mM NH_3 in phosphate buffer (pH=10.86) to demonstrate the activity of our catalysts. The tested sample did not contain nitrate or nitrite, which shows that the plain electrode is not capable of oxidizing ammonia.

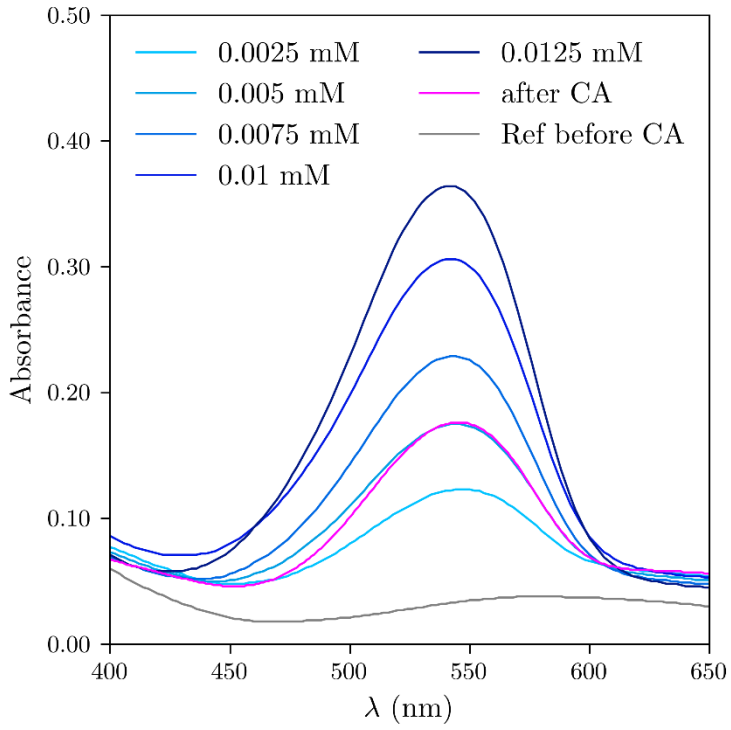

Figure S 33: UV/VIS spectrum of an anode solution after CA after Zn dust reduction and adding 2 mL C (pink) and the KNO_3 standard solutions after adding1.5 mL of solution C (blue).

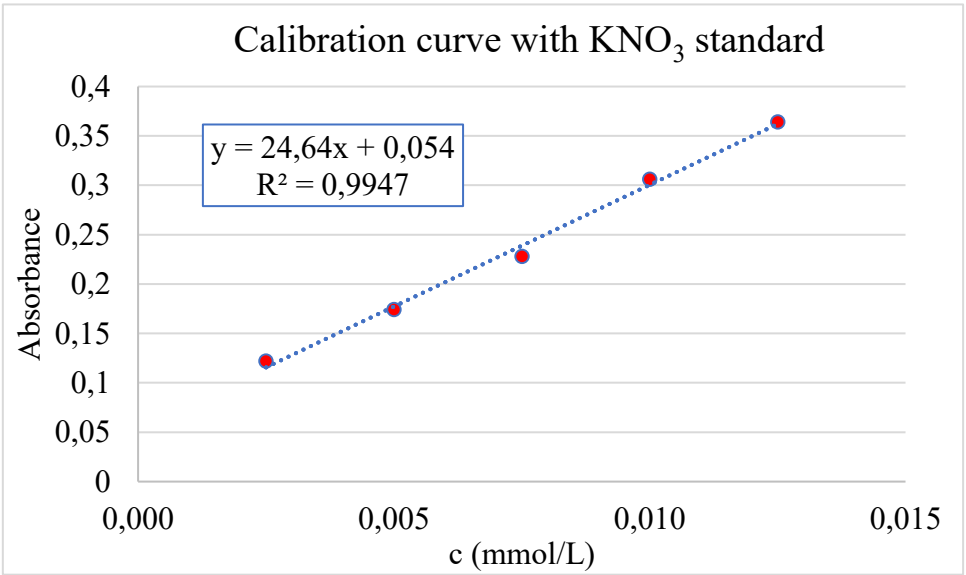

Figure S 34: Calibration curve of the nitrate standard (mmol/L) after adding 1.5 mL A of solution C.

Calculations

$$NH_4^+ + 2H_2O \longrightarrow HNO_2 + 7H^+ + 6e^- \quad \textbf{(eq. 3)}$$

$$NH_4^+ + 3H_2O \longrightarrow NO_3^- + 10H^+ + 8e^- \quad \textbf{(eq. 4)}$$

Table S 8: Measured and calculated values for guest **1** after 90 min CA at 0.5V in 200 mM NH_3 phosphate buffer in H_2O (pH= 10.86) measured three times.

Guest 1	M1	M2	M3	average
Absorbance	0,194	0,143	0,176	
c(NO_3^-)(mmol/L)	0,011	0,0073	0,010	
Q (C)	0,0414	0.0265	0,0315	
FE	96%	95%	98%	**96%**

Table S 9: Measured and calculated values for guest **2** after 90 min CA at 0.5V in 200 mM NH_3 phosphate buffer in H_2O (pH= 10.86) measured three times.*

Guest 2	M1	M2	M3	average
Absorbance	0,109	0,134	0,089	
c(NO_3^-)(mmol/L)	0,0052	0,0098	0,0043	
Q (C)	0,0237	0.0480	0,0434	
FE	68%	94%	45%	**69%**

***Guest 2** exhibited differing values when repeated multiple times and we assume that this is due to the lower stability of the complex in aqueous solution at higher pH and the, inconsistent surface loading in different experiments.

Inserting the measured absorbance in the related calibration curve gives the concentration in mmol/L.

In an example, the following values are calculated:

$$\boldsymbol{Q = nFN} \quad \textbf{(eq. 5)}$$

Q= charge passed (C)

n= number of electrons (6 or 8)

N= mol

$$\textbf{c2 } (\textbf{NO}_3^-) = \frac{0.0057\left(\frac{mmol}{L}\right)\times 0.00402\ L}{0.002\ L} = 0.01142\ mmol/L$$

0.0057 mmol/L is calculated from the calibration curve: y (Absorbance) = 24.64x + 0.054 → (0.176 - 0.054)/24.64 = 0.0057 mmol/L; 0.00402 (V_1= 2 mL anode solution + 2 mL color reagent C + 20 µL HCl= 0.00402 L)

V= **V**anode solution -**V**taken for test = 0.0065L - 0.002L= 0.0045L

$$\textbf{N } (\textbf{NO}_3^-) = 0.01142\left(\frac{mmol}{L}\right) \times 0.0045\ L = 5.2\ \cdot 10^{-5}\ mmol$$

$$\boldsymbol{Q_{NO_3-}} = 8 \times 96485.33\left(\frac{C}{mol}\right) \times 5.2\ \cdot 10^{-8}\ mol = 0.040\ C$$

$$\textbf{FE}= \frac{Q_{NO2-} + Q_{NO3-}}{Q_{experimental}} \times 100 = \frac{(0+0.040C)}{0.04143C} \times 100 = 96\% \quad \textbf{(eq. 6)}$$

NH_3 concentration studies in H_2O

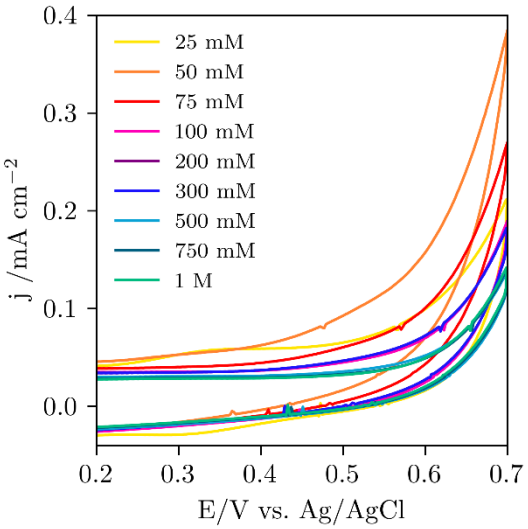

Figure S 35: Concentration studies of NH_3 in aqueous ammonia solution (0.2 M $NaClO_4$, 20 mVs^{-1}). Conditions: WE: mITO+H+G, CE: Pt wire, RE: AgCl wire in 0.2M $NaClO_4$ in H_2O.

Nitrate characterization with ^{14}N NMR

As an additional characterization method, ^{14}N NMR of the anode solution after electrocatalysis of both guests was measured (pH= 10.8), 10% D_2O was added to the anode solution.

a)

Anode solution after 90 min CA

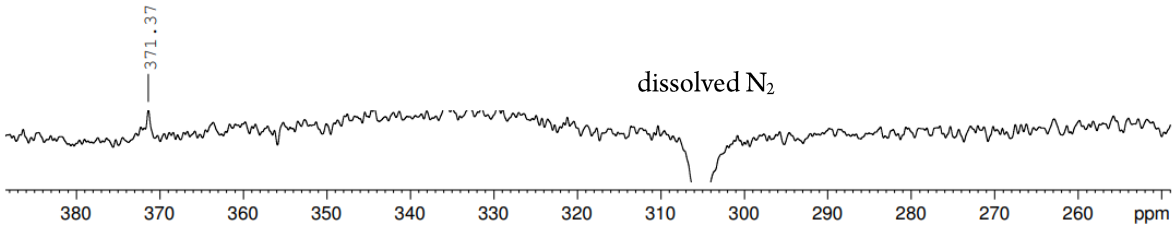

b)

Reference: $HNO_3 + NH_4OH$ in phosphate buffer (pH >11)

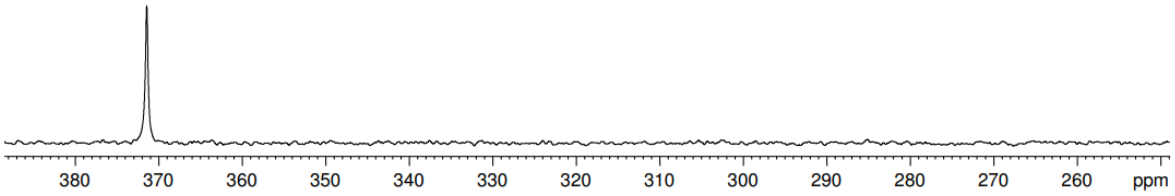

Figure S 36: ^{14}N NMR of the anode solution after electrocatalysis in 200 mM NH_3 in phosphate buffer (pH= 10.86) of the guest (a) and a reference sample (b), the samples were diluted with 10% D_2O. The signal at 306 ppm can be assigned to dissolved N_2 (from the air) in the samples and is traceable in all measurements including the reference.

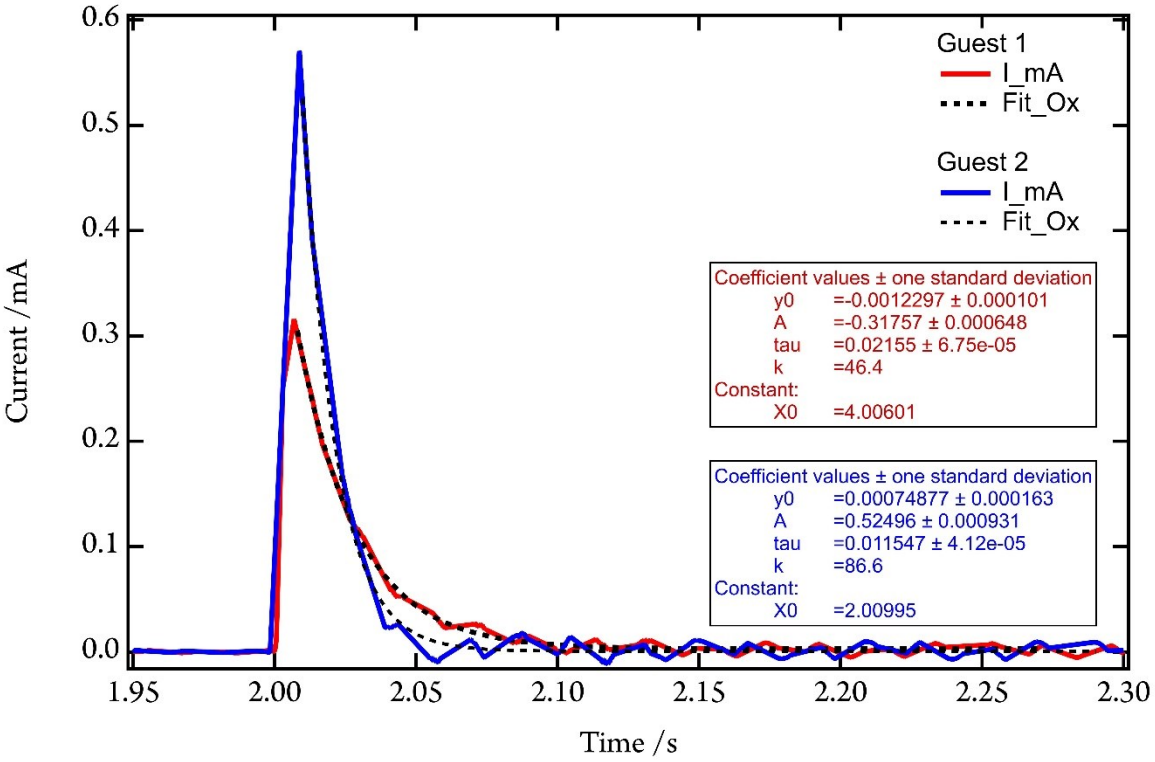

Figure S 37: Fast CA from 0.02 to 0.2 V in 10 steps of compound 1. The graphs show one representative example (20 mV vs. V_{OC}) with the corresponding fit for guest **1** (red) and guest **2** (blue). Conditions: WE: mITO+ Guest **1**, CE: Pt wire, RE: AgCl wire in 0.2M $NaClO_4$ in H_2O measured in 0.5M NH_3 in water solution.

To determine the electron transfer rate from the catalyst to the surface, fast CA was performed. For that purpose, potential steps from 0 to a certain potential and back were performed to the oxidative and the reductive potential in 10 steps from 0.02 to 0.2 and from -0.02 to -0.2, respectively. The resulting data of each step were plotted, and the sum of all measured potentials was analyzed to determine the rate transfer.

Fitting of the current after a positive voltage step of 40 mV from Voc.

The fitting procedure used was an exponential decay:

$$f(x) = y_0 + A * e^{\left\{\frac{-(x-x_0)}{\tau}\right\}} \qquad \textbf{(eq. 7)}$$

With y_0 and x_0 as the y and x offset, A as constant, and τ (s) as time constant for the decay. τ itself is the inverse of the decay rate constant, which in turn is the sum of the forward and backward reaction rate constant k_f+k_b (s^{-1}) as defined by Chidsay.[13]

Reabsorption studies after electrocatalysis in THF

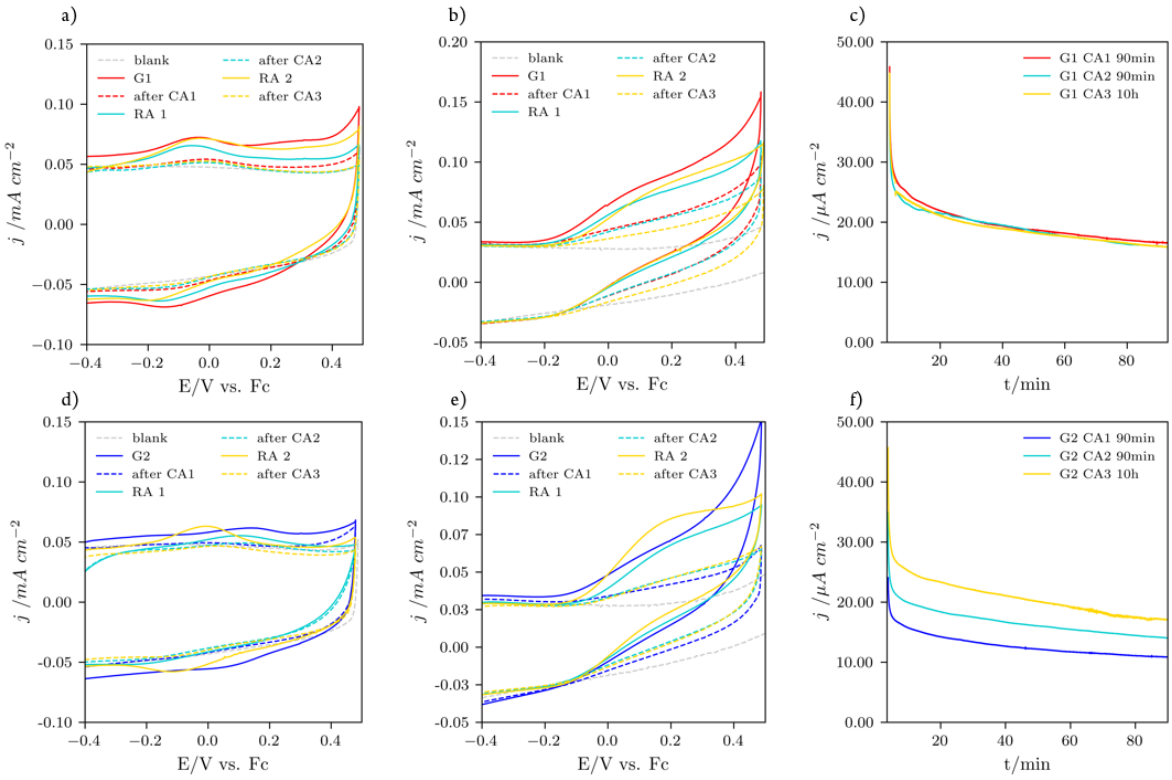

Figure S 38: Electrochemistry of guest **1** (G1, red) and guest **2** (G2, blue) and reabsorption of guests after CA (turquoise and yellow) before (solid line) and after (dashed line) CA. a,d) CV (100 mVs^{-1}) in 0.1 M $TBAPF_6$ in THF before (solid line) and after CA (dashed line), b= blank (dashed grey line, WE: mITO+H) and b,e) CV (20 mVs^{-1}) in 0.1 M $TBAPF_6$ and 0.1 M NH_4PF_6 in 0.5 M NH_3 in THF. c,f) CA for twice 90 min followed by 10h (shown only 90 min window) at 0.1 V (vs Fc). Conditions: WE: mITO+H+G, CE: Pt wire, RE: AgCl wire in 0.1 M $TBAPF_6$ in THF.

The potential of the reference electrode shifts when exposed to ammonia solution for several hours. That explains the shift of the redox peak in the third guest reabsorption (yellow).

Reabsorption studies after electrocatalysis in aqueous solution

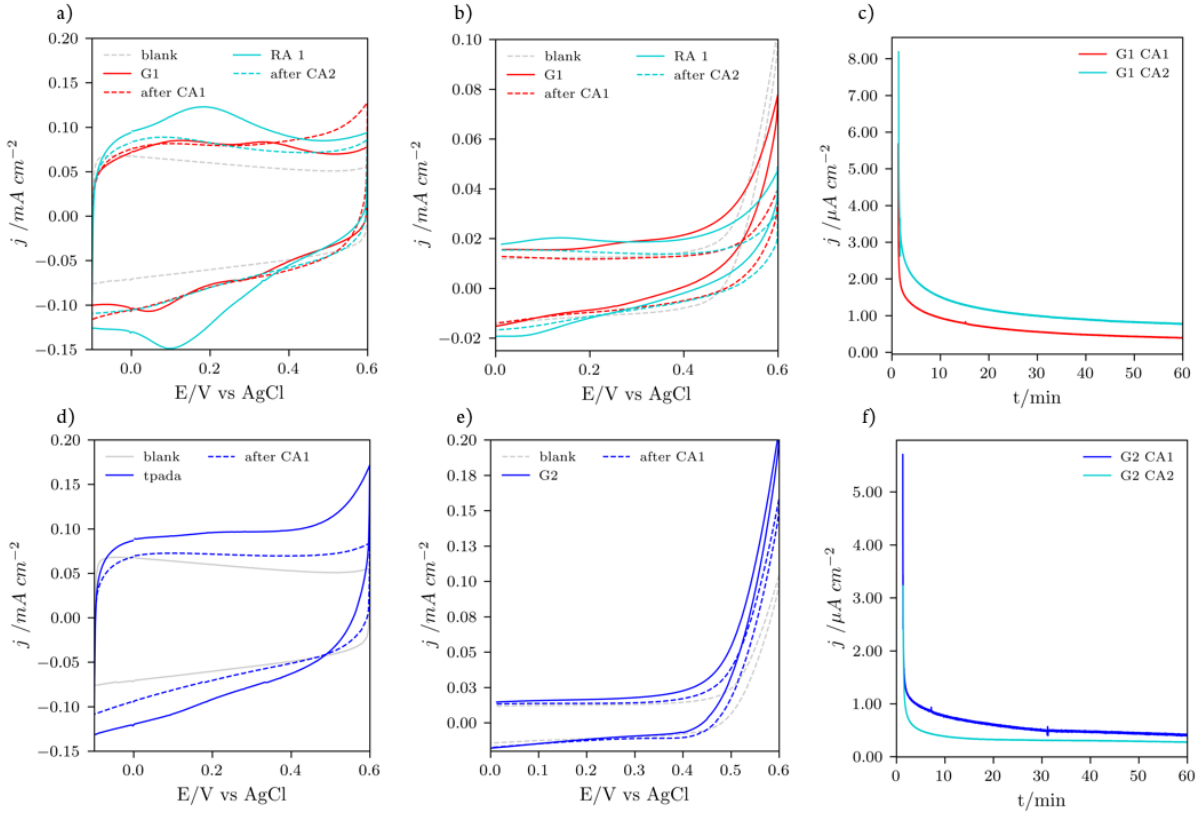

Figure S 39: Electrochemistry of guest **1** (G1, red) and guest **2** (G2, blue) and reabsorption of guests after CA (turquoise) before (solid line) and after (dashed line) CA. a,d) CV (100 mVs^{-1}) in 0.2 M $NaClO_4$ in H_2O before (solid line) and after CA (dashed line), b= blank (dashed grey line, WE: mITO+H) and b,e) CV (20 mVs^{-1}) in 0.5 M NH_3 in H_2O (pH= 11.4, 22°C). c,f) CA for twice 60 min at 0.2 V (turquoise) and 0.3 V (red, blue) (vs Ag/AgCl). Conditions: WE: mITO+H+G, CE: Pt wire, RE: AgCl wire in 0.2 M $NaClO_4$ in H_2O.

Reabsorption with guest exchange studies after electrocatalysis in aqueous solution

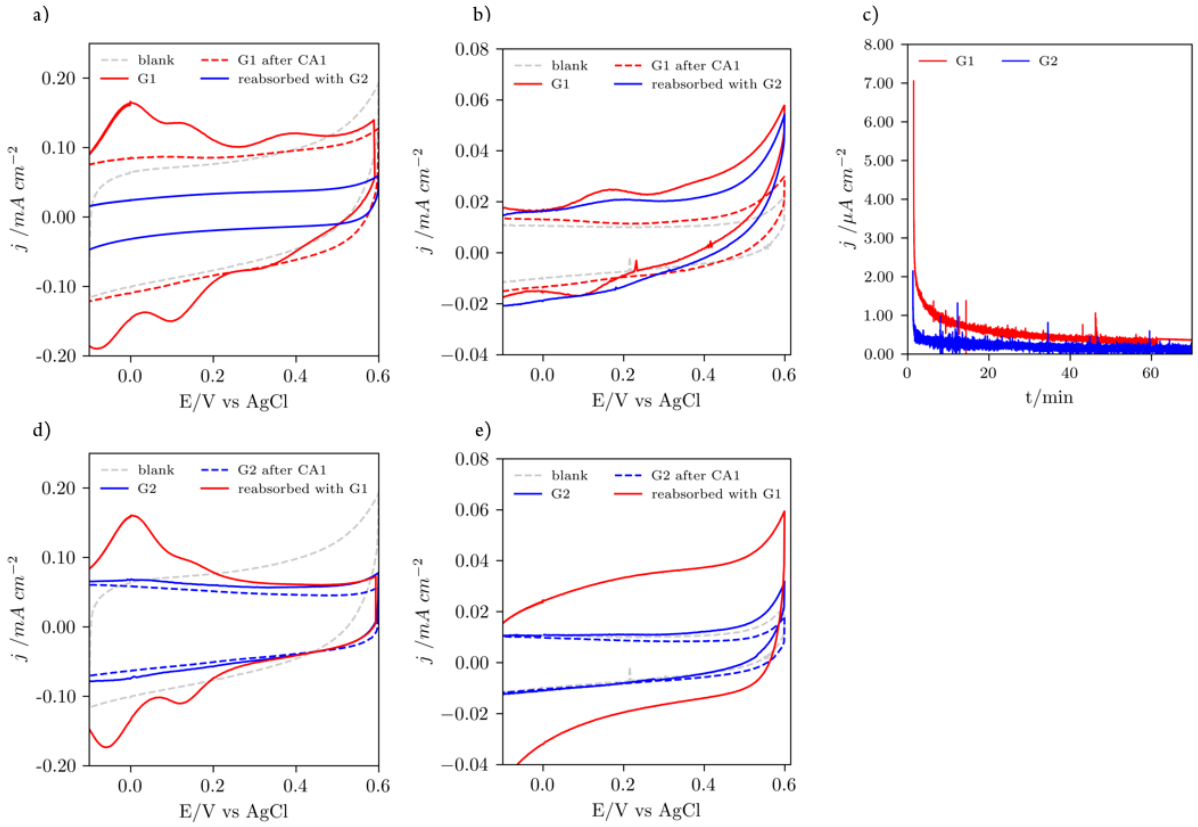

Figure S 40: Electrochemistry of guest **1** (G1, red) and guest **2** (G2, blue) and reabsorption of guests after CA. a,d) CV (100 mVs^{-1}) 0.1 M phosphonate buffer in H_2O (pH= 8.16 at 21ºC). before (solid line) and after CA (dashed line), b= blank (dashed grey line, WE: mITO+H) and b,e) CV (20 mVs^{-1}) in 2M NH_3 in 0.1 M phosphonate buffer in H_2O (pH= 10.8 at 21ºC). c) CA for twice 70 min at 0.2 V (vs AgCl). Conditions: WE: mITO+H+G, CE: Pt wire, RE: AgCl wire in 0.2 M $NaClO_4$ in H_2O.

The reabsorption of the respective other guest molecule was demonstrated with cyclic voltammetry. The adamantane guest **1** (red) shows strongly pronounced redox peaks in water and ammonia solution and can be replaced with the naphthalene guest **2** (G2, blue), in the second cycles after G1 is decomposed during catalysis (red dashed line, a and b upper row). The same process can be performed with first naphthalene and reabsorption of the adamantane guest G1, red (a and b, below).

References

[1] Sévery, L.; Szczerbiński, J.; Taskin, M.; Tuncay, I.; Nunes, F. B.; Cignarella, C.; Tocci, G.; Blacque, O.; Osterwalder, J.; Zenobi, R.; Iannuzzi, M.; David Tilley, S. Immobilization of Molecular Catalysts on Electrode Surfaces Using Host-Guest Interactions. https://doi.org/10.1038/s41557-021-00652-y

[2] *CrysAlis^{Pro} Software system*; Rigaku Oxford Diffraction, vers. 1.171.42; Rigaku Corporation, 2022.

[3] G. M. Sheldrick, *Acta Cryst.* **2015**, *A71*, 3.

[4] G. M. Sheldrick, *Acta Cryst.* **2015**, *C71*, 3.

[5] O. V. Dolomanov, L. J. Bourhis, R. J. Gildea, J. A. K. Howard, H. Puschmann, *J. Appl. Cryst.* **2009**, *42*, 339.

[6] C. F. Macrae, L. Sovago, S. J. Cottrell, P. T. A. Galek, P. McCabe, E. Pidcock, M. Platings, G. P. Shields, J. S. Stevens, M. Towler, P. A. Wood, *J. Appl. Cryst.* **2020**, *53*, 226.

[7] A. L. Spek, *Acta Cryst.* **2015**, *C71*, 9.

[8] H. Wu, R. Andres, Q. Wang and J. Zhu, *Angewandte Chemie International Edition*, 2019, **58**, 499–503.

[9] C. Constable, N. Hostettler, C. E. Housecroft, P. Kopecky, M. Neuburger and J. A. Zampese, *Dalton Transactions*, 2012, **41**, 2890.

[10] http://app.supramolecular.org/bindfit/

[11] Bühler, J.; Zurflüh, J.; Siol, S.; Blacque, O.; Sévery, L.; Tilley, S. D. Electrochemical Ruthenium- Catalysed C–H Activation in Water through Heterogenization of a Molecular Catalyst. Catal Sci Technol 2022, 12 (5), 1512–1519. https://doi.org/10.1039/D1CY01999F.

[12] Han-Yu Liu, Hannah M. C. Lant, Jennifer L. Troiano, Gongfang Hu, Brandon Q. Mercado, Robert H. Crabtree, and Gary W. Brudvig, *Journal of the American Chemical Society* **2022** *144* (19), 8449-8453. DOI: 10.1021/jacs.2c01788

[13] Chidsey, C. E. D. Free Energy and Temperature Dependence of Electron Transfer at the Metal-Electrolyte Interface. *Science (1979)* **1991**, *251* (4996), 919–922. https://doi.org/10.1126/science.251.4996.919.